Characteristics of continental rifting in rotational systems: New findings from spatiotemporal high resolution quantified crustal scale analogue models

Timothy C. Schmid [a,*], Guido Schreurs [a], Jürgen Adam [b]

[a] *Institute of Geological Sciences, University of Bern, Baltzerstrasse 1+3, Bern CH-3012, Switzerland*
[b] *Earth Sciences Department, Royal Holloway University of London, Egham TW20 0EX, United Kingdom*

A B S T R A C T

Continental rifts are the expression of regional horizontal stretching and are in modelling studies often assumed to be the result of orthogonal or oblique extension. However, naturally occurring V-shaped rift geometries infer an underlying rotational component, resulting in a divergence velocity gradient. Here we use such analogue models of rifting in rotational settings to investigate and quantify the effect of such a divergence velocity gradient on normal fault growth and rift propagation towards a rotation pole. Particularly, we apply different divergence velocities and use different brittle-ductile ratios to simulate different crustal configurations and analyse its effect on rift propagation and surface deformation. Surface deformation is captured using stereoscopic 3D Digital Image Correlation, which allows for quantifying topographic evolution and surface displacement including vertical displacement. In combination with X-Ray computed tomography, we gain insights into the three-dimensional structures in our two-layer models. Based on our models, we present a novel characterisation of normal fault growth under rotational extension which is described by 1) an early stage of bidirectional stepwise growth in length by fault linkage with pulses of high growth rates followed by a longer and continuous stage of unidirectional linear fault growth; 2) segmented rifting activity which promotes strain partitioning among competing conjugate faults and 3) along-strike segmented migration of active faulting from boundary faults inwards to intra-rift faults allowing different fault generations to be simultaneously active over the entire rift length. For models with higher divergence velocities, inward migration is delayed but other first-order observations are similar to models with lower divergence velocities. Our quantitative analysis provides insights on spatiotemporal fault growth and rift propagation in analogue models of rotational rifting. Although natural rifts present complex systems, our models may contribute to a better understanding of natural rift evolution with a rotational component.

1. Introduction

The understanding of continental rifting has greatly improved over the last century by field studies, geophysical techniques, and analogue and numerical modelling. While geophysical approaches are strongly limited to present-day conditions, the modelling approach has the advantage to demonstrate rifting processes over a wide temporal and spatial extent. In the case of experimental modelling techniques (Overview in review article from Corti (2012)), examples of such temporal and spatial evolution are inward migration of faulting (as the result of progressive extension in narrow rifts), fault linkage and rift interaction as well as rift propagation.

Inward rift migration describes the process of progressive narrowing of tectonic activity towards the rift axis. In this process, tectonic activity and related basin subsidence move from large boundary faults inwards to intra-rift faults where subsidence results in second generation intra-rift subbasins (e.g., Agostini et al., 2009; Corti, 2012; Corti et al., 2013; Corti et al., 2010; Ebinger, 2005). Inward rift migration represents a temporal strain partitioning between early boundary faults and late stage intra-rift faults (Ebinger, 2005).

Other modelling studies have investigated lateral fault growth and fault linkage (e.g., Bellahsen et al., 2003a; Bellahsen and Daniel, 2005; Schlagenhauf et al., 2008) as well as rift segment linkage structures (e.g., Allken et al., 2011, 2012; Brune, 2014; Brune et al., 2017; Corti et al.,

---

2019; Glerum et al., 2020; Koehn et al., 2008; Zwaan and Schreurs, 2017, 2020; Zwaan et al., 2016). In addition, analogue modelling studies have investigated vertical fault growth and fault linkage in brittle-ductile strata (e.g., Gabrielsen et al., 2016; Gabrielsen et al., 2019; Vasquez et al., 2018).

For quantifying fault growth, attempts have been made in the past based on the geometric relation between fault length and maximum displacement (see Walsh and Watterson, 1988; Watterson, 1986). However, such a model lacks kinematic considerations on how faults grow over time in length and accumulate displacement (Walsh et al., 2002). More recently, two coexisting conceptual models suggest fault growth by either (1) linear growth in which fault length and displacement synchronously accumulate by fault linkage and propagation (i.e., propagating model; Cartwright et al., 1995; Walsh and Watterson, 1988; Watterson, 1986) or (2) by an initial phase of rapid propagation followed by a longer phase of displacement accumulation along at near constant fault length (i.e., constant length model; Jackson and Rotevatn, 2013; Nicol et al., 2005; Rotevatn et al., 2019; Schlagenhauf et al., 2008; Walsh et al., 2002). Rotevatn et al. (2019) consider the propagating, and the constant length models to be end members and suggest a hybrid fault growth model in which initial rapid fault lengthening occurs by fault linkage and lengthening followed by a stage of constant length displacement accumulation. Indeed, the kinematic interaction of fault segments and its importance for effective rift propagation has been discussed in numerous studies (e.g., Morley et al., 1990; Morley, 1999; Nelson et al., 1992; Schlische, 1992). In early stages of rifting, the rift boundary faults rapidly grow laterally by linkage of numerous small faults. After the early lateral fault growth, the boundary faults focus on fault displacement accumulation generating tectonic subsidence in the longitudinally continuous rift.

Although conceptual fault growth models may be supported by observations from modelling studies using orthogonal extension (Bellahsen et al., 2003a; Schlagenhauf et al., 2008), fault growth under rotational extension has not yet been studied in similar detail. Therefore, it remains unclear how individual fault segments in rotational settings accumulate strain and how a gradient in divergence velocity does influence fault linkage contributing to the propagation of the entire rift system.

To answer these questions, we present 3D analogue models of continental rifting in rotational systems on a crustal scale and analyse fault growth and rift propagation at different divergence velocities. We apply 3D stereo Digital Image Correlation (DIC) for the quantitative analysis of the surface deformation in 3D. In addition, X-ray computed tomography is used to qualitatively analyse internal model deformation and fault evolution. By a combination of novel imaging techniques to capture surface deformation and a detailed quantification analysis of individual structures we present novel insights on crustal scale deformation in rifts with an along-strike divergence velocity gradient.

2. Natural examples and analogue models of plate rotation

Although various modelling studies use constant divergence velocities along the strike of a rift system to examine propagating rifts (e.g., Le Pourhiet et al., 2018; Michon and Merle, 2000; Van Wijk and Blackman, 2005), in nature often significant velocity gradients occur along the strike of diverging plate boundaries because of their rotational plate motion around a vertical rotation pole (Euler pole; Martin, 1984; Smith, 1993).

Numerous rotational rift settings have been proposed for example for the Red Sea (e.g., Bonatti, 1985; Souriot and Brun, 1992) and the Gulf of Aden region because of a counter clockwise rotation of the Arabian plate (e.g., Bellahsen et al., 2003b). In the Laptev Sea, the Gakkel Ridge forms a symmetric spreading ocean ridge, where spreading rates gradually decrease towards the present-day rotation pole near the coast of the Laptev Sea (Dick et al., 2003; Sekretov, 2001; Van Wijk and Blackman, 2005). Another setting in which rotational basin opening has been proposed is the aligned Rockall Trough, Faeroe Basin and Møre Basin in

the Northeast Atlantic (e.g., Doré et al., 1999; Hanisch, 1984; Lundin and Doré, 1997). More illustrative compilations of rift settings with rotational extension are given in Zwaan and Schreurs (2020) and Zwaan et al. (2020).

In the case of back-arc extension, subduction slab retreat velocity may vary along the trench resulting in asymmetrical spreading and a block rotation component (e.g., Schellart et al., 2002; Wallace et al., 2009; Wallace et al., 2005). A spectacular example of this process can be found in the Southern Rhodope Core complex in the Aegean, where southward retreat of the Hellenic subduction zone resulted in a regional clockwise rotation up to 50°-60° around a pole located at Scutary-Pec, Albania (Brun and Sokoutis, 2010) and triggered the exhumation of the triangular shaped Southern Rhodope Core Complex (SRCC; Brun and Sokoutis, 2007). Analogue models with boundary conditions adapted to the Aegean back-arc extension provide first-order explanation of the mechanical evolution of the Rhodope core complexes (e.g., Kydonakis et al., 2015; Philippon et al., 2014).

Other analogue modelling studies of asymmetric back-arc extension that involve block rotation investigated the Tonga-Kermadec arc system in the Southwest Pacific (Schellart et al., 2002), the Kuril Basin in the Northwest Pacific (Schellart et al., 2003), or the Havre Trough near the southern Kermadec Trench (Benes and Scott, 1996). In the latter case, the rift propagates from the Southern Havre Trough into the continental lithosphere at the northern margin of New Zealand forming the Taupo Rift Zone (Fig. 1). The Taupo rift provides an excellent recent natural example of rotational opening due to its juvenile rift stage and high extension rates (e.g., Villamor et al., 2017). East of the North Island, the Pacific plate is subducted under the Australian plate along the Hikurangi Trough. Further to the south, the collision of the Chatham Rise (a buoyant continental fragment) with the Hikurangi Trough eventually ceases subduction and exerts a torque on the crustal blocks leading to a clockwise tectonic block rotation around a vertical rotation pole near the Chatham Rise (e.g., Nicol and Wallace, 2007; Wallace et al., 2004; Wallace et al., 2009; Wallace et al., 2005; Fig. 1 inset).

Most recent analogue modelling studies of rotational rifting intensively investigated the interaction of propagating rifts and linear mantle heterogeneities (Molnar et al., 2017; Molnar et al., 2019) and their role in forming microcontinents (Molnar et al., 2018). Subsequently, Khalil et al. (2020) used more complex heterogeneities to investigate rifting in the Afar region. At crustal scale, Maestrelli et al. (2020) examined the interaction of propagating rifts and pre-existing brittle crustal fabrics. Furthermore, Zwaan and Schreurs (2020) analysed rift interaction of linear crustal weaknesses as a function of rift underlap and compared their findings with models of orthogonal extension.

Although the abovementioned recent modelling studies improve our understanding of overall rift propagation in rotational settings, a detailed and quantitative analysis of fault growth is missing. Therefore, the crustal-scale models presented here focus on a spatially and temporally high resolution analysis on individual fault growth which ultimately controls rift propagation in a rotational rift setting.

3. Methods

3.1. Experimental apparatus

Our experimental machine simulates rotational extension and has been used and described in previous studies by Zwaan and Schreurs (2020) and Zwaan et al. (2020). For the sake of completeness, we briefly describe the modelling approach here. The model setup is confined by two short, curved sidewalls and long mobile sidewalls (Fig. 2). The two mobile sidewalls are pivoting around a vertical rotation axis separating the model box into a 65 cm long extensional and 25 cm long contractional domain, respectively (Fig. 2a,b). The applied divergence velocity is defined by the opening of the distant circular segment in the extensional domain and linearly decreases towards the rotation axis. Hence, no deformation occurs at the rotation axis and largest deformation
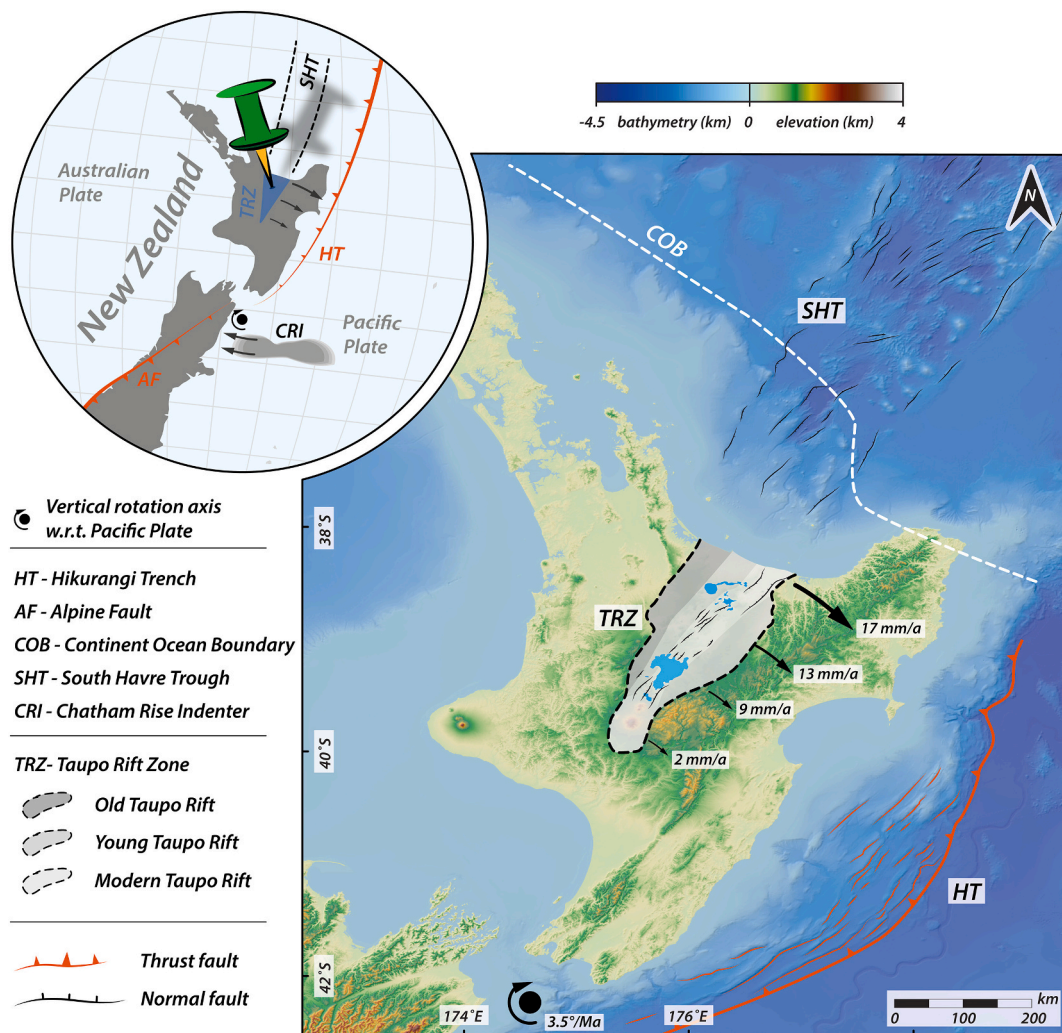
Fig. 1. Structural segmentation of the Taupo Rift Zone (TRZ) and the subduction margin of the Hikurangi Trough (HT). The Taupo Rift Zone is chronologically segmented into Old, Young and modern Taupo Rift. GPS and field data (Nicol and Wallace, 2007; Wallace et al., 2004) depicts a clear divergence velocity gradient along the rift axis from the NW end towards SE . At the continent-ocean boundary (COB), the Southern Havre Trough (SHT) advances into the continental Taupo Rift Zone. Inset: Geodynamic configuration of the Australian and Pacific Plates near New Zealand with the transition from continental collision along the Alpine Fault (AF) to subduction and back-arc extension along the Hikurangi Trough and Southern Havre Trough.. Collision of the buoyant Chatham Rise Indenter (CHI) and the Hikurangi trench causes a clock wise rotation of the North Island. Topography and bathymetry are obtained from the ASTER DEM version 3 and GEBCO (2021), respectively. Coordinate system is WGS84. Faults are schematically redrawn after Nicol and Wallace (2007).

occurs at distant model parts. Subsequently, we use the terms distal and proximal to refer to rift-axis parallel deformation in the extensional domain further away and closer to the rotation axis, respectively. Fig. 3 shows extension and shortening in our model box as a function of time and distance to the rotation pole. Assuming no deformation localization, (i.e., no heterogeneities) this can be used as a proxy for model deformation. Note, that stretching and shortening are not linear over time and space.

The initial model area is defined by a quasi-rectangular surface with gently curved, short side walls with a maximum length of 90 cm along the central axis and a width of 31 cm. For our analyses, we leave out the outermost, curved model parts resulting in a rectangular area of interest of about 80 by 31 cm. The model sits on top of a 5 cm thick foam base which is initially compressed between the longitudinal sidewalls. Rotational movement results in stretching of the foam below the extensional domain and further shortening of the foam below the contractional domain. To prevent the model from sinking in, the foam base is supported by vertical plexiglass bars (Fig. 2d). Therefore, the basal model boundary does not accommodate for isostatic contribution from the mantle. However, our models focus on crustal deformation

which, in return, allows for a better spatial resolution necessary for our analyses. To ensure that the brittle cover is decoupled from the base setup by the viscous layer (i.e., excluding potential boundary effects due to the basal setup), we run 2D DIC analyses on surface top view images of the basal setup (supplementary fig. S1).

3.2. Analogue model setup

The two-layer model consists of a brittle-viscous set up with a brittle layer sitting on top of a viscous layer. The brittle layer simulates the upper crust, whereas the viscous layer simulates the ductile lower crust (Fig. 2c). To localise rifting within the brittle layer, we apply "seeds" (semi-cylindrical PDMS/corundum sand mixture rods with radius of ca. 0.5 cm) along the entire model length on top of the viscous mixture. These seeds act as an inherited heterogeneity and have been successfully implemented in analogue models of previous rifting studies (e.g., Molnar et al., 2020; Zwaan and Schreurs, 2020; Zwaan et al., 2019; Zwaan et al., 2020). The rift location can be controlled by a reactivation of pre-existing weaknesses or basement fabric (e.g., Collanega et al., 2018; Corti, 2012; Heilman et al., 2019; Seebeck et al., 2014). In this light, our
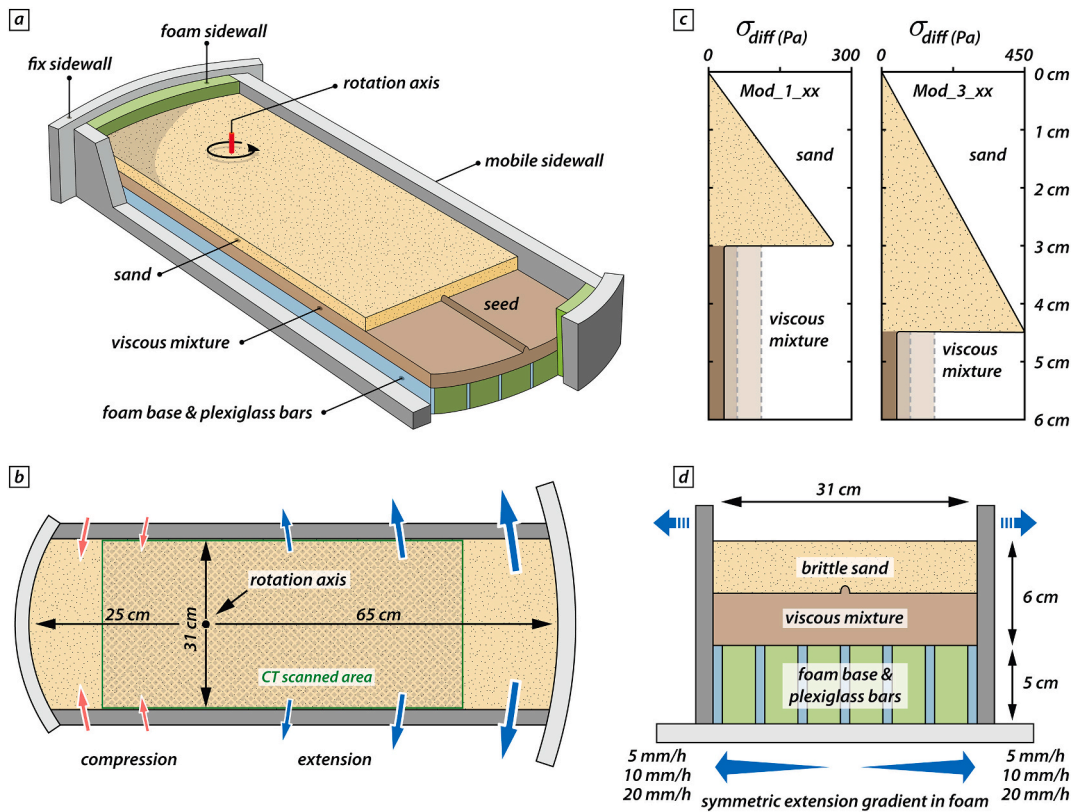
Fig. 2. Model setup for conducted experiments. (a) Cut-out view of the experimental apparatus. The model is confined by two curved short walls and long movable side walls. The laundry-peg like apparatus defines a compressional and an extensional domain separated by a rotation axis. (b) Top view of the experimental apparatus. The rotation axis causes a velocity gradient with increasing distance. The green rectangle indicates CT scan coverage of model Mod_1_10_CT. c) Schematic strength profile for the two-layer setup with a brittle ductile ratio $R_{BD} = 1$ (left) and $R_{BD} = 3$ (right). Different shading of the viscous layer refers to viscous strength increase with increasing divergence velocities. d) The model setup consists of a brittle sand layer representing the upper brittle crust on top of a viscous mixture of PDMS and corundum sand imitating the lower ductile crust. The two-layer model sits on top of a foam base that extends homogeneously after compression prior to the experiment run. The foam base is supported by plexiglass bars to prevent the model from sinking in.
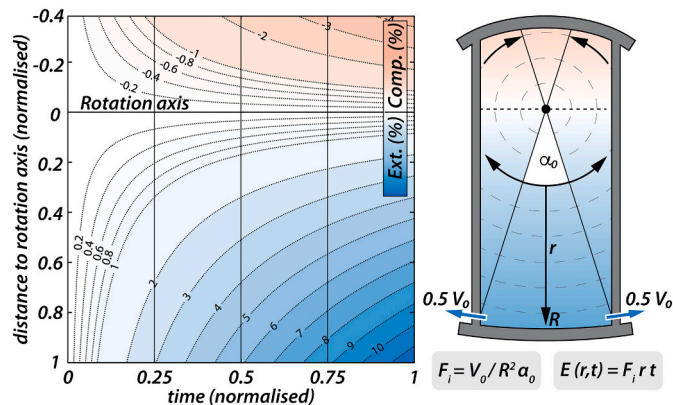Modified from Zwaan et al. (2020).

Fig. 3. Calculated extension and shortening values for the model domain as a function of time and distance, relative to the rotation axis. Applied maximum divergence velocity V_0 is defined by the opening of the distant circular segment with maximum radius R. For all conducted models, maximum bulk extension values are around 12%.

seed is a structural weakness that can become reactivated allowing the rift to develop and propagate preferentially above it. For visual aid, a fine 4 by 4 cm grid of corundum sand is sieved on the model surface prior to the model run whereas random patterns of coffee powder sprinkled on the surface act as passive markers facilitating further quantitative DIC

analysis.

We focus at the documentation and deformation analysis on a reference model with an overall thickness of 6 cm, representing a 30 km thick continental crust, with a brittle-ductile ratio $R_{BD} = 1$ and an applied maximum divergence velocity of 10 mm/h (i.e., the divergence velocity furthest away from the rotation axis), similar to the initial setup used in Zwaan et al. (2020). However, in order to check the robustness of our findings and interpretation, we conduct a series of analogue models in which we systematically change divergence velocities to investigate the influence of different extension rates on rift propagation and fault growth (Fig. 2,c). In addition, different divergence velocities are applied in models with two different thickness ratios R_{BD} to simulate different initial crustal configurations. Namely, $R_{BD} = 1$ and $R_{BD} = 3$, representing intermediate (models Mod_1_xx) to high (models Mod_3_xx) crustal strength respectively, in a stable cratonic lithosphere dominated by brittle deformation. Note that "xx" denotes the applied maximum divergence velocity. In total we run a series of nine models of which six models examine the abovementioned parameters. In addition, we re-run models using the reference setup of model Mod_1_10 for CT scans (Mod_1_10_CT) and a model excluding the contractional domain (Mod_1_10_EXT). Additionally, we run a model with a brittle ductile ratio $R_{BD} = 2$ (Mod_2_10). All models are listed in.

For our reference experiment (hereafter Mod_1_10), the mobile sidewalls open with a maximum divergence velocity of 10 mm/h (symmetrically 5 mm/h each side), linearly decreasing towards the rotation axis. After a total run time of four hours, this results in a maximum extension of 40 mm or about 13% maximum extension.

Similarly, maximum shortening of 15.4 mm or 5% is reached at the final stage at the distant circular segment in the contractional domain. We double the maximum divergence velocity to 20 mm/h (10 mm/h on each side; models Mod_1_20 and Mod_3_20) and further increase it to 40 mm/h (20 mm/h on each side; models Mod_1_40 and Mod_3_40) to subsequently increase the lower ductile crustal strength and enhance brittle-ductile coupling. We keep the amount of bulk extension similar by changing the model run time from 4 h (Mod_1_10 and Mod_3_10) to 2 h (Mod_1_20 and Mod_3_20) and 1 h (Mod_1_40 and Mod_3_40) to compare all models.

3.3. Analogue material

For the viscous basal layer, we use a mixture of corundum sand and polydimethylsiloxane (PDMS) with a mixing ratio 1:1. The mixture has a density of 1600 kg/m^3 and a viscosity of ca 1.5·10^5 Pa s with a quasi-linear stress exponent of 1.05 (Zwaan et al., 2018). As an analogue for the upper brittle crust, we use dry loose quartz sand with a bulk density Table 1 of 1560 kg/m^3. This density is achieved by sieving sand into the model box from a height of 30 cm. Thus, a proper density gradient is assured to avoid density driven upwelling of the viscous mixture. During the experiment, localised deformation in the quartz sand layer locally lowers the initial friction coefficient. This strain softening is quantified as the difference between the coefficient of peak friction and dynamic friction coefficient divided by the reactivation friction coefficient (Panien et al., 2006) from mutual two-point regression analysis. For quartz and corundum sands, strain softening values are 16% and 18%, respectively and are derived from friction coefficients in Schmid et al. (2020a, 2020b).

For a CT scanned experiment, we add small quantities (weight ratio 1:50) of Zirshot ceramic microbeads to the quartz and corundum sands to enhance volumetric patterns on CT scans to facilitate DVC analysis (Adam et al., 2013). In addition, a 1 mm thin layer of corundum sand is sieved from 30 cm height on top of the viscous mixture before adding quartz sand to enhance the X-ray absorption contrast between the viscous and brittle domain. The influence of the ceramic microbeads and the thin corundum sand layer on the overall mechanical properties is minor and can be neglected (Klinkmüller, 2011; Panien et al., 2006;

Table 1
Overview of different models with varying brittle-ductile ratio and divergence velocity.

Model name	Brittle ductile ratio R$_{BD}$	Max. divergence velocity (mm/h)	Comment
Mod_1_10	1	10	Reference model
Mod_1_20	1	20	
Mod_1_40	1	40	
Mod_1_10_CT	1	10	CT scanned model
Mod_1_10_EXT	1	10	Extensional domain only model
Mod_2_10	2	10	
Mod_3_10	3	10	
Mod_3_20	3	20	
Mod_3_40	3	40	

Schmid et al., 2020a). All relevant material properties are summarized in Table 2.

3.4. Scaling

In order to ensure proper scaling of our models up to natural scales we apply the standard equations based on Hubbert (1937) and Ramberg (1981). For brittle Mohr-Coulomb type materials dynamic similarity is given by the equation for stress ratios

$$\sigma^* = \rho^* g^* h^* \tag{1}$$

By convention, σ^* is defined as:

$$\sigma^* = \sigma^m / \sigma^n \tag{2}$$

where m and n represent model and nature, respectively. Further, ρ^*, g^* and h^* represent the density, gravity, and length ratios, respectively. Our reference setup yields a geometric scaling factor of $h^* = 2 * 10^{-6}$, a density scaling factor of $\rho^* = 0.58$, and a gravity scaling factor of 1, resulting in a stress scaling factor of $\sigma^* = 10^{-6}$. With a cohesion around 50 Pa and 50 MPa for our quartz sand and upper crustal rocks (Byerlee, 1978) respectively, the cohesion scaling factor is $c^* = 10^{-6}$.

The strain-rate ratio $\dot{\epsilon}^* = 8*10^9$ for viscous materials is obtained from the stress ratio σ^* and the viscosity ratio $\eta^* = 2 * 10^{-16}$ (Weijermars and Schmeling, 1986):

$$\dot{\epsilon}^* = \sigma^* / \eta^* \tag{3}$$

Next, the velocity ratio v^* and the time ratio t^* are calculated with

$$\dot{\epsilon}^* = \frac{v^*}{h^*} = \frac{1}{t^*} \tag{4}$$

with a velocity scaling ratio $v^* = 2 * 10^4$ and a time ratio $t^* = 10^{-10}$.

Based on our scaling, 1 cm in our experiments corresponds to 5 km in nature. For an intermediate lower crustal viscosity of $\eta = 10^{21}$ Pa s (Zwaan et al., 2019 and references therein), one hour in our analogue experiments translates to about 0.88 *Ma* in nature and the reference extension velocity (10 mm/ h) converts to a velocity of 5–6 mm a^{-1} and strain-rate values of 6 10^{-15} s^{-1} in nature, close to typical values for initial continental rifting (Zwaan et al., 2019). Our experiments cover strain rates varying by a factor of 4 (5 * 10^{-5} s^{-1} - 2 * 10^{-4} s^{-1}), which translates to a variation by a factor of about 3 in nature (6 * 10^{-15} s^{-1} - 2 * 10^{-14} s^{-1}).

For verifying dynamic similarity of brittle natural and experiment material we calculate the Smoluchowski number S$_m$, which is the ratio between gravitational stress and cohesive strength (Ramberg, 1981):

$$S_m = \frac{\rho g h}{C + \mu \rho g h} \tag{5}$$

where , h, C and μ are the density, thickness, cohesion, and friction coefficient, respectively of the brittle material. With a cohesion of 50 MPa and friction coefficient of ca 0.6 (Byerlee, 1978) for upper crustal rocks, this yields a S$_m$ around 1 for our models as well as for nature. We further calculate the Ramberg number R_m to ensure dynamic and kinematic similarities between the viscous layers.

Table 2
Material properties.

Granular materials	Quartz sand	Corundum sand	Zirshot	Viscous material	PDMS/corundum mixture
Density (kg/m^3)	1560 (30 cm)	1960 (30 cm)	2300 (bulk)	Density (kg/m^3)	1600
Grainsize (µm)	60–250	88–175	150–210	Viscosity (Pa s)	1.5 10^5
Friction coefficient µ	0.72	0.78		Stress exponent n	1.05
Angle of internal friction°	36	38			
Strain softening (%)	16	18			
Cohesion (Pa)	48 ± 26	55 ± 42			

$$R_m = \frac{\rho g h^2}{\eta v} \qquad (6)$$

For the reference velocity, this yields a Ramberg number of 34 and 36 for our models and nature, respectively. The Reynolds number R_e is defined as the ratio between inertial forces to viscous forces and is for all our models as well as for the natural prototypes $<< 1$:

$$R_e = \frac{\rho v h}{\eta} \qquad (7)$$

Note, that we use the maximum extension velocity (i.e. the velocity furthest away from the rotation axis) for calculating R_m and R_e. In most parts of our experiments, however, velocities are smaller due to the velocity gradient. While $R_e << 1$ remains valid for the entire extensional domain, R_m increases with decreasing velocities towards the rotation axis. In the middle of the extensional domain, R_m is around 68 while halving the velocity yields a Ramberg number of about 71 for nature. However, the ratio between model and nature Ramberg number remains close to 1 within the entire velocity range. Based on the applied scaling laws, the material properties and the similar non-dimensional numbers for model and nature, we consider the reference model to be properly dynamically scaled. Reference model parameters and dynamic numbers of the used materials are specified in Table 3. Note that for varying divergence velocities and brittle ductile ratios scaling factors and dynamic numbers change. However, changes are minor, and we consider them to be negligible.

3.5. Deformation monitoring

We use a customised automated light and camera setup as shown in Fig. 4 with selectable image interval allowing us to take images for qualitative top view analysis as well as stereo images for 3D surface and displacement analysis by means of 3D stereo DIC (Adam et al., 2005). The surface evolution is captured with time-series images by three DSLR cameras in 60 s intervals. A Nikon D200 (10.2 Mpx) is used for top view images and two Nikon D810 (36 Mpx) cameras in stereoscopic setup, are used for 3D surface deformation monitoring. All cameras are aligned above the model surface with the top view camera in middle position above the model centre and two cameras with an inclination angle of ca. 30 degrees with respect to each other for stereoscopic images. Two LED light sources with a colour temperature of 4000 K illuminate the model surface from two opposing sides to avoid shadow casting. For top view images, however, only one light source is active to enhance visibility of surface deformation structures. In order to switch automatically between these two light settings, a digital timer controls one LED light source in a 30 s on/off cycle. The top view camera is automatically controlled and passes its image trigger signal onto a programmable ESPER TriggerBox that retains the signal for 30 s before transferring it to the stereoscopic camera setup. This delay is necessary to change light settings. Hence, images are sequentially taken every 60 s but with a shift of 30 s between top view and stereoscopic images.

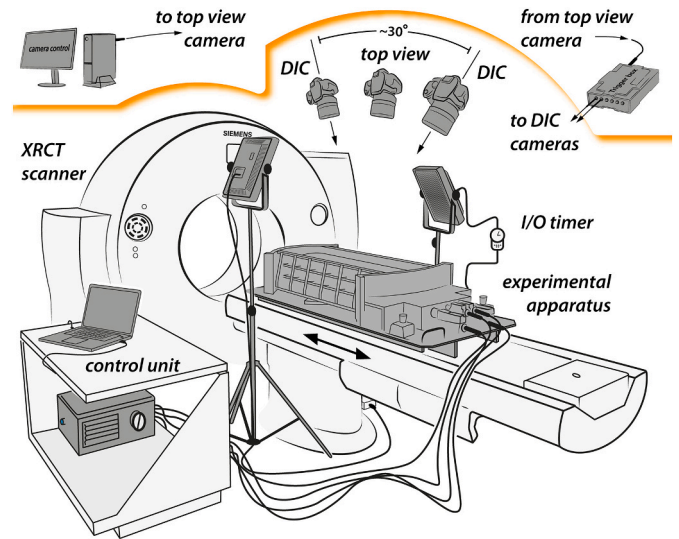For recording model internal deformation, we rerun our reference

Fig. 4. Experimental setup for 3D stereo DIC monitoring and CT scanning. The model box sits on a slidable table and is scanned every 20 min within a medical XRCT device. Surface evolution is captured by a one-minute interval with three DSLR cameras. Stereo cameras for 3D surface monitoring are aligned on top of the model with an angle of ca. 30 degrees with respect to each other. A camera for top view images is placed in the middle between the stereo cameras. The top view camera is controlled by a software and takes surface pictures in a distinct interval. This signal is held back by the trigger box and released half an interval later to activate the stereo cameras. The camera cycle is synced with two light sources which illuminate the model surface for 3D surface monitoring and a single light source for top view images to cast shadows for enhancing surface structures. Sidewall velocities of the model box are adjusted and paused for scanning by the control unit.

model Mod_1_10 in a medical XRCT scanner (64 slice Siemens Somatom Definition AS X-ray CT-scanner), hereafter called Mod_1_10_CT. This model is scanned at 20 min interval (every 3.3 mm of maximum extension or 1% extension) for a total experiment duration of 240 min. In addition, rerunning Mod_1_10 with identical setup allows to assess experimental reproducibility. The scan resolution is 512 by 512 pixels for each slice with a scan window of 37 by 37 cm. The applied scan protocol is resource intensive and consequently we limit the scan area to a horizontal 68 by 31 cm rectangle (Fig. 2b).

3.6. Data analysis and post processing

Tools and techniques to quantify deformation in analogue models have greatly improved in the last decades. Digital Image Correlation (DIC) is a non-destructive method for quantitative deformation analysis, which has been successfully applied for high-resolution analysis of 2D, 3D surface and 3D volume analysis of localised and diffuse deformation in analogue experiments (Adam et al., 2013; Adam et al., 2005; Zwaan

Table 3

Scaling parameters and scaling factors based on reference model Mod_1_10. Note that for calculating R_m the maximum velocity is used.

	General parameters			Brittle upper crust		Ductile lower crust		Dimensionless numbers		
	Gravity [m/s²]	Crustal thickness [m]	Extension velocity [m/s]	Density [kg/m³]	Cohesion [Pa]	Density [kg/m³]	Viscosity [Pa s]	Smoluchowski Sm	Ramberg Rm	Reynolds Re
Model	9.81	$6 \; 10^{-2}$	$2.8 \; 10^{-6}$	1560	50	1600	$1.5 \; 10^{5}$	1	34	$<<1$
Nature	9.81	$3 \; 10^{4}$	$1.4 \; 10^{-10}$	2700	$5 \; 10^{7}$	2900	$1 \; 10^{21}$	1	36	$<<1$

Scaling factors $x^* = x^m/x^n$ [dimensionless]								
σ^*	ρ^*	g^*	h^*	c^*	$\dot{\epsilon}^*$	η^*	v^*	t^*
$1 \; 10^{-6}$	0.55	1	$2 \; 10^{-6}$	$1 \; 10^{-6}$	$8 \; 10^{9}$	$2 \; 10^{-16}$	$2 \; 10^{4}$	$1 \; 10^{-10}$

et al., 2017). 2D DIC using a single camera (map or profile view) to compute 2D displacements and strain fields is a widespread technique applied on analogue models of tectonic processes (Schellart and Strak, 2016) and free software MATLAB toolboxes are available for analysis (e. g., Boutelier, 2016; Boutelier et al., 2019; Thielicke and Stamhuis, 2014). More advanced commercial software makes it possible to use stereoscopic camera arrangements and directly compute the 3D topography and 3D displacement vector field of the deforming experiment surface (e.g., 3D Stereo Digital Image Correlation (DIC); Adam et al. (2005)).

3.6.1. 3D Stereo Digital Image Correlation (3D Stereo DIC)

Here, we use the StrainMaster module from the commercial DaVis image correlation software (version 8.4, LaVision). This method combines stereoscopic DIC techniques with volume mapping to quantify the 3D surface topography and respective 3D displacement fields from time-series stereo images (Adam et al., 2005; Krézsek et al., 2007). This workflow includes 3D volume calibration (camera calibration and mapping function for image correction and surface height), static measurement of the surface shape (scalar field calculation from stereo image pairs for topography based on mapping function M′), and dynamic measurement of 3D surface deformation (calculation of 3D displacement field on surface from time-series stereo images). For displacement calculation, DaVis uses a least square matching algorithm with adaptive multi-pass cross-correlation. For local displacement calculations we utilise subsets (interrogation windows) of 31 by 31 pixels with a 75% overlap. The analysed model areas consist of ca. 6500 by 2500 pixels for the x- and y-axis, respectively with an average volume calibration misfit of ca. 0.6 pixels. With an average pixel size of ca. 0.1 mm, volume calibration yields absolute residual fit errors of about 0.06 mm. For topography and displacement field calculations the average reconstruction error is 0.4 and 0.05 mm, respectively. Once displacement fields are calculated postprocessing evaluates, discards, and interpolates unreliable vectors. We use a peak ratio Q < 2 to validate uniqueness of vectors. More precisely, if a correlation peak value is less than twice the second peak value, the vector is discarded. Additionally, a universal outlier filter is applied to check for specious vectors within a 3 by 3 neighbourhood (Westerweel and Scarano, 2005). Discarded vectors in the displacement fields are replaced by an iterative interpolation requiring at least two neighbouring vectors. When summing up incremental displacement fields flow advection due to applied velocities are considered by using the Lagrangian sum of displacements (Boutelier et al., 2019).

Displacement fields are exported as DaVis inherent .vc7 files and further processed as .h5 files with MATLAB (version 18b). Using small strain approximation, the strain tensor E is obtained from displacements with:

$$E_{ij} = \frac{\partial v_i}{\partial x_j} \tag{8}$$

with the components,

$$E = \begin{bmatrix} E_{xx} & E_{xy} \\ E_{yx} & E_{yy} \end{bmatrix} \tag{9}$$

where E_{xx} and E_{yy} are the normal strain components in x and y directions, respectively and E_{xy} and E_{yx} are the shear components. Note, that for symmetrical tensors (i.e., non-rotational) $E_{xy} = E_{yx}$. The maximum principal stretching axis (largest eigenvalue) defines the maximum normal strain, E_{surf}, on the surface and is expressed as:

$$E_{surf} = \frac{E_{xx} + E_{yy}}{2} + \sqrt{\left| \frac{(E_{xx} - E_{yy})^2}{4} + \frac{(E_{xy} + E_{yx})^2}{4} \right|} \tag{10}$$

Eq. (10) is useful to express strain in our rotational experiments, as E_{surf} is independent of the coordinate system.

To enhance signal to noise ratio in incremental displacement fields, all incremental entities are further smoothened by averaging with the two previous and two subsequent incremental displacement fields (i.e., averaging over 5 min). For all displacement derived top view maps we use the Scientific colour maps package from Crameri (2018).

3.6.2. Data post-processing

For an in-depth analysis, we further postprocess 3D stereo DIC data by applying the workflow shown in Fig. 5. The stereoscopic camera setup allows to obtain spatially high-resolution digital surface elevation models at any desired interval. For each conducted experiment, eleven topographic cross-sections perpendicular to the rift axis, track deformation in 10% intervals of the model length (i.e., 2%, 10%, 20%, …, 90%, 98%; Fig. 5a). During the experiment runs, a data base is built up consisting of 2651 topographic profile lines (i.e., 11 × 241, including initial topography profiles). Due to the rigid basal setup our models are not isostatically compensated. Consequently, applied bulk extension homogeneously thins the viscous layer even so in the absence of localised deformation. Such homogenous thinning of the viscous layer results in an artificial regional subsidence which must be considered. We therefore use MATLAB (Ver. 2018 b) to correct topographic profiles by filtering out the effect of this regional subsidence. Fig. 5 shows the workflow of correcting topographic profiles. The along-strike profile P12-P12′, indicated by the red dashed line (Fig. 5a,b), highlights the regional subsidence in the extensional domain that occurs away from the developing rift. To analyse vertical displacement features such as local rift shoulder uplift, we correct topographic profiles perpendicular to the long axis of the model (e.g., section P4-P4′ in Fig. 5a). By treating each value of the surface height as a function of the spatial position within the profile line (i.e., H(x) + C) with C being a constant value indicating the regional subsidence (Fig. 5c), its numerical differential (dH/dx) yields change in topography due to faulting (Fig. 5d). By applying the inverse function (i.e., the improper numerical integral), we back calculate the original shape of the function H(x) ignoring the regional subsidence C (Fig. 4e). Further, we track a strain value threshold of 10% along the boundary faults to quantify growth of single faults of the rift system (supplementary fig. S2). Note that we do not consider sedimentation nor erosion which would massively impede fault growth analysis and rift propagation examination otherwise.

4. Results

We have conducted in total nine analogue models investigating the influence of variable maximum divergence velocities and brittle ductile ratios on rift propagation, fault growth and fault interaction in rotational rift settings. The first-order rift evolution, in terms of fault patterns, fault orientation as well as temporal and spatial relation, displays strong similarities in all our models. Therefore, we present the results in this section based on our reference model Mod_1_10 and consider them to be representative for the general evolution of deformation in our models. Inarguably, alterations of second-order features occur when changing initial conditions and must be discussed. Hence, we compare all models with our reference model in the discussion and take them into account for our conclusion.

4.1. Qualitative rift evolution

After ca. 5 mm of maximum extension (at the distal part in the extensional domain), initial deformation structures of the nascent rift become visible at the surface (Fig. 6a,e). A CT cross section image from model Mod_1_10_CT (Fig. 6i) indicated by the red line (Fig. 6e) shows a first set of conjugate faults which corresponds to the boundary fault segments in model Mod_1_10 (Fig. 6e) at this stage. These extensional faults strike orthogonal with respect to the extension direction and show a steep dip angle of about 70°. At the brittle/viscous boundary these fault planes unite at the tip of the viscous seed. Faults in surface view
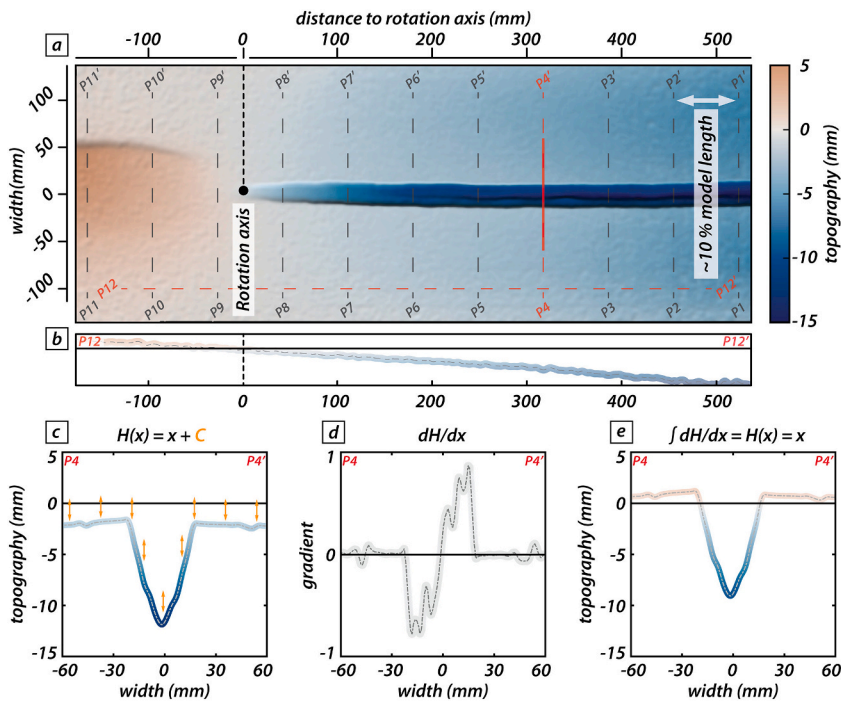
Fig. 5. Workflow for obtaining subsidence-corrected profiles of the model topography. a) Example of surface data obtained from stereoscopic DSLR camera setup. Parallel to the short axis 11 surface topography cross sections are taken aligned approximately every 10% of the analysed surface over 241 min (including initial topography). b) Topography-profile along the long model axis (at width = −100 mm) visualizing the gradually increasing subsidence along the rift axis due to the boundary conditions. c) The uncorrected topography profile is expressed by a function H(x) and a constant value indicating the regional subsidence at the given position. d) Discrete difference function representing the gradient of the topography dH/dx. Note that the constant value vanished. (e) Corrected topography profile obtained by the discrete summation of dH/dx.

develop either as distinctive short, segmented faults (Fig. 6e) or as long continuous faults, propagating towards the rotation axis over time. The conjugate extensional faults establish an early graben structure and further extension is localised on these two rift faults; hereafter called rift boundary faults. After 15 mm extension, early isolated fault segments are entirely connected building a continuous rift basin with widths of about 3 to 4 cm (Fig. 6b,f,j). After 20 mm extension, further deformation has accumulated along the boundary faults while additionally a new fault forms in the centre of the rift basin (Fig. 6c,g,k). Conjugate boundary faults gently rotate from an original dip angle of 70° to 60° and a set of newly formed conjugate faults (hereafter called intra rift faults) becomes visible in the CT scan images (Fig. 6k). Note that the black arrows in CT cross sections indicate zones of upward flow of the viscous mixture (see discussion Section 5.1). Contemporaneously, in the contractional domain initial surface deformation indicates thrust faulting (Fig. 6c,g). At around 26.6 mm extension, the pair of conjugate normal faults, formerly only visible in CT scan images, fully develops in the hanging wall of the rift boundary faults forming a central intra-rift graben localising further extensional deformation (Fig. 6d,h,l). Fig. 7 shows the final stage after 40 mm extension, where the rift propagated towards the rotation axis. At this stage the rift boundary faults are completely linked and delimit a first-generation graben structure. In the central part of the rift zone, second-generation conjugate intra-rift normal faults form an intra-rift graben, which expresses further localised subsidence. At the latest stage, weakly visible third-generation extensional faults initiate and indicate the potential formation of a future minor intra-rift basin (Fig. 7a,b). The migration of active faulting in the rift centre that can be inferred from the gradual increase of subsidence towards the rift axis is clearly visible in our model. In the contractional domain, at a maximum contraction after 240 min, two conjugate thrusts appear forming a pop-up structure.

4.2. Quantitative rift evolution

In addition to the qualitative description of top view images, maps of various displacement components derived from 3D stereo DIC enable the quantitative analysis and visualisation of displacement distribution, subsidence, and localised strain patterns. We use incremental as well as

cumulative (i.e., dt = 60 s for the reference model Mod_1_10) vertical displacement components, dz. and Dz, respectively to show the temporal and total subsidence. Incremental strain-rates obtained from incremental displacement field data are used to derive incremental maximum normal strain-rate values (i.e., the maximum principal stretching rate) to reveal fault activity. Identical time intervals as shown for the qualitative analysis (Figs. 6 and 7) are used for the quantitative model description.

4.2.1. Cumulative vertical displacement (Dz)

Fig. 8 shows the cumulative vertical displacement field for the same extension values as shown in Figs. 6 and 7. Note that values are not corrected for regional subsidence, resulting in a wider area of diffuse subsidence and uplift in the extensional and contractional domains, respectively. After 5 mm of maximum extension (Fig. 8a), the two conjugate boundary faults separate undeformed domains of minor subsidence and a distinct graben with maximum total subsidence (Dz) of ca. 4 mm. After 15 mm extension (Fig. 8b), total subsidence within the rift has increased to ca. 8 mm. Both rift boundary faults propagated towards the rotation axis and total subsidence within the rift decrease towards the rotation axis. Across from the rotation axis, a diffuse zone of uplift defines the early stages of contraction. At 20 mm maximum extension (Fig. 8c), localised subsidence within the rift zone gradually increases. Intra rift faults become visible at 400 mm with respect to the rotation axis. In the contractional domain, uplift is limited to a narrower area with a step in the uplift values marking the surface expression of thrust faults. Between 20 mm and 30 mm of maximum extension (Fig. 8c,d,e), intra rift faults further propagate towards the rotation axis. In the contractional domain, thrusting results in uplift up to 5 mm in the central part (i.e., between −50 and 50 mm model width). At the final state (Fig. 8f), both boundary faults have reached the rotational axis. It is noteworthy, that the evolution of distinct deformation features takes place in the earlier stages of the model with successive displacement accumulation in later stages.

4.2.2. Incremental vertical displacement (dz)

Incremental vertical displacement dz. describes the active subsidence and uplift movements in a specific time interval, and therefore, allows the distinction of major and minor phases of uplift and
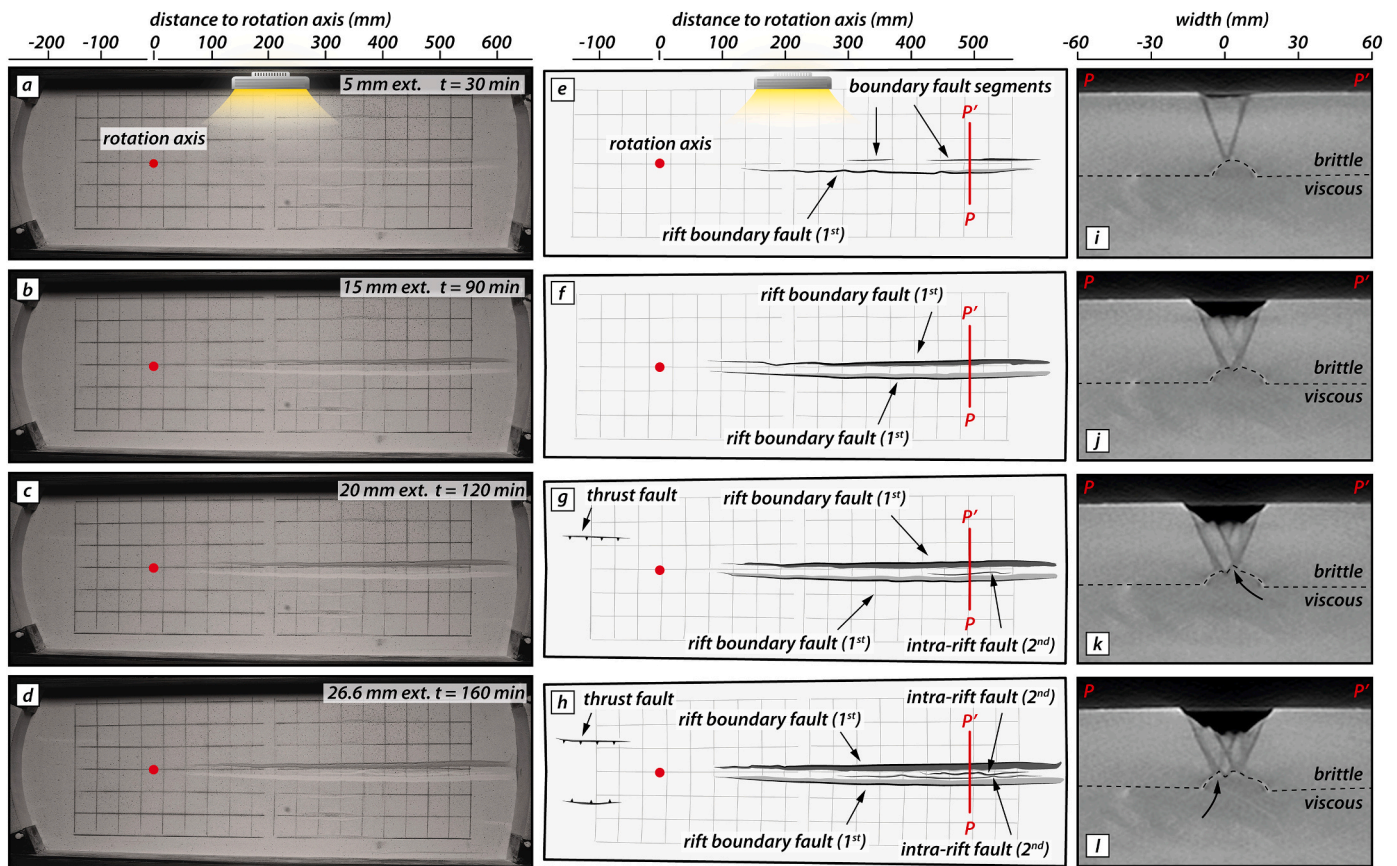
Fig. 6. Surface evolution of model Mod_1_10 and XRCT cross-sectional slices of model Mod_1_10_CT at positions indicated by profile P-P'. a-d) Top view images of selected time steps at 30, 90, 120 and 160 min. e-h) Surface key features for the selected time steps. i-l) XRCT image slices from model Mod_1_10_CT at the indicated profile line. After 30 min of the model run, first surface structures are visible as two rift-boundary faults form (a,e,i). An initial graben structure is bounded by discontinuous south-dipping boundary fault segments and a continuous north-dipping fault. After 90 min, single fault segments are linked and form a pronounced rift with two continuous boundary faults confining a deepening graben structure (b,f,j). The fault tips propagate towards the rotation axis as further deformation is taken up by the two boundary faults. After 120 min, new north-dipping fault segments form within the existing graben structure (c, g,k). Across the rotation axis first thrust faults form within the contractional model domain. After 160 min, north-dipping as well as south-dipping faults form a central second order graben within the two existing rift-boundary faults. More shortening is taken up by the south-dipping thrust fault across the rotation axis (d,h,l). Black arrows in CT slices highlight advancing viscous tips.

subsidence. Fig. 9 shows the temporal sequence of incremental vertical displacement. Note that sharp colour contrasts in the subsidence indicate active faults. After 5 mm extension (Fig. 9a), active subsidence is distributed over the entire rift zone with subsidence rates up to 0.1 mm per minute at distal model parts indicating homogeneous and uniform subsidence of the rift graben structure at rift transects (i.e., both rift boundary faults take up similar amounts of vertical displacement). The subsidence rate changes linearly from maximum vertical displacement rates of 0.1 mm per minute from the distal extension domain to zero close to the rotation axis. After 5 mm extension, both rift boundary faults have taken up similar amounts of total vertical displacement of about 2 mm (see Fig. 8a). In this early rift stage, uplift in the contractional domain occurs in a broad and diffuse fashion, although increased values of uplift in the centre are visible. Propagation of the rift boundary faults becomes evident after 15 mm extension (Fig. 9b). The well-defined incremental subsidence pattern propagates towards the rotation axis forming a continuous graben structure in between the rift boundary faults. After 20 mm extension (Fig. 9c), however, the rift-wide uniform subsidence pattern changes towards more localised subsidence in the rift centre in the distal rift zone (about 400 to 500 mm with respect to the rotation axis). The localisation of subsidence along this section indicates the transfer of fault displacement from the major boundary faults towards intra rift faults in the rift centre. After 26.6 mm extension (Fig. 9d), fault activity along both boundary faults decreased at the

distal extension domain and further vertical displacement is taken up by a pair of conjugate intra rift faults. However, both boundary faults are still active closer to the rotation axis. Considering the divergence velocity gradient, boundary faults at the distal end reflect a more mature rift stage and experience inward fault migration first. In the final stage (Fig. 9e), incremental vertical displacement shows that the pair of conjugate boundary faults is still active near the rotation axis and at a distant zone (300–500 mm), a pair of conjugate intra rift faults are active. Vertical displacement in the distal rift zone is narrowed down and indistinguishable. The fault segment activity for the final model stage is illustrated in Fig. 9f.

4.2.3. Incremental maximum normal strain rate on surface (e_{surf})
The temporal sequence of fault activity is analysed using incremental strain rate maps obtained from the maximum surface strain E_{surf}. In the first 5 mm of extension, the first generation of fault segments (rift boundary faults) are observed in the strain-rate maps as well-localised continuous linear features (Fig. 10a). After 15 mm extension, the boundary faults remain active, but a second-generation conjugate set of intra rift faults is indicated by new fault trends with moderate strain-rate values in between the rift boundary faults (Fig. 10b). After 20 mm extension, second-generation fault segments (intra rift faults) develop in between the two existing conjugate normal faults in the distal extension domain shown by increasing strain-rates along these fault trends
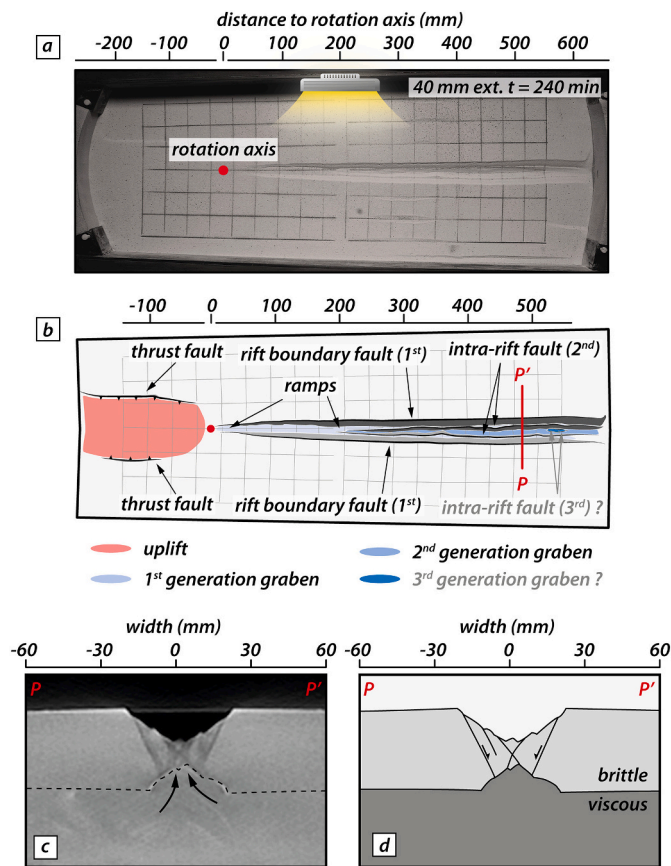
Fig. 7. Surface and corresponding XRCT image slices of the final model stage after 240 min. a) Top view image. b) Key features of the model evolution. The initial rift boundary faults propagated to the rotation axis and bound a first-generation graben structure. In the central part of the rift, second-generation faults form an internal second-generation graben which continues to accumulate subsidence. A small basin has formed at the eastern end of the rift forming a minor third generation graben. Across the rotation axis an area of uplift is bounded by thrust faults. Red solid dot indicates rotation axis. c) XRCT image slice from model Mod_1_10_CT at the indicated profile line. . Black arrows highlight advancing viscous tips. d) Sketch of XRCT image slice.

(Fig. 10c). Strain-rate values of the rift boundary faults drop (and therefore activity) as intra rift faults develop in between indicating progressive migration of fault activity on intra rift structures. The second-generation intra rift faults propagate as conjugate normal faults towards the rotation axis similar to the first-generation rift boundary faults. As intra rift faults grow and accumulate strain, strain-rate values along the rift boundary faults locally decrease (Fig. 10d) indicating fault abandonment. At the final stage, in the distal rift zone activity along third-generation faults is shown by localised strain-rate values in the rift centre (Fig. 10e). It is notable that at this stage, activity along 3rd generation faults is documented in the incremental strain rate data (Fig. 10e) but not yet in the incremental vertical displacement map, yet (Fig. 9e,f).

4.3. Strain rate distribution for models with varying maximum divergence velocities and brittle ductile-ratios R_{BD}

Fig. 11 shows strain rate maps (i.e., incremental maximum normal strain rate on surface) for identical maximum extension values used to present the fault evolution of the reference model. For models with a brittle-ductile ratio $R_{BD} = 1$ (Mod_1_10, Mod_1_20 and Mod_1_40), activation of successive fault generations (i.e., intra-rift faults) is subsequently stalled with increasing divergence velocities (Fig. 11a).

Therefore, activity of 3rd generation faults is limited to model Mod_1_10 with a maximum divergence velocity of 10 mm/h. This also holds for models with a brittle-ductile ratio $R_{BD} = 3$ (Mod_3_10, Mod_3_20 and Mod_3_40; Fig. 11b), where faulting mainly occurs along 1st generation rift boundary faults. The activation of 2nd generation faults is for all conducted divergence velocities limited to late stages of the model runs and 3rd generation faults are entirely absent. Moreover, models with different brittle-ductile ratios differ in average rift width (i.e., the distance between conjugate rift boundary faults at the model surface). For a brittle-ductile ratio $R_{BD} = 1$, the average rift width is about 30 mm, whereas for models with a ratio $R_{BD} = 3$, the average rift width is about 50 mm. The increase in rift width is a geometric effect of the thicker brittle layer in models with ratio $R_{BD} = 3$. In addition, higher velocities models (Mod_1_20, Mod_1_40, Mod_3_20 and Mod_3_40) show increased boundary effects towards the end of the model runs, indicated by oblique zones of increased strain rate values near the curved model boundary in the extension domain.

5. Discussion

The gradient in rift maturity towards the rotation axis reflects the imposed velocity gradient and is an essential and common aspect in models investigating rotational rifting (see Khalil et al., 2020; Maestrelli et al., 2020; Molnar et al., 2017; Molnar et al., 2020; Molnar et al., 2018, 2019; Zwaan and Schreurs, 2020; Zwaan et al., 2020). Indeed, our models confirm first-order observations and show similarities when compared with previous analogue modelling studies of rotational rifting. Our reference model Mod_1_10 is in strong agreement with the rotational model series presented in Zwaan et al. (2020). This is expected since we use a similar setup here. Similarly, we use a central weak "seed" on top of the viscous layer to localise faulting along a central rift system facilitating the detailed study of fault growth and rift propagation. Maestrelli et al. (2020) use for their crustal scale models a brittle-ductile ratio $R_{BD} = 1$ and maximum divergence velocities of 20 mm/h, like our model Mod_1_20. However, their model setup has two fundamental differences. In contrast to localised deformation in our models, Maestrelli et al. (2020) use a rubber sheet at the base of the viscous layer producing distributed deformation expressed by fault swarms. In addition, Maestrelli et al. (2020) examine the influence of inherited fabrics in the brittle model part crosscut by a propagating rift (see also Zwaan and Schreurs (2020)). Analogue modelling studies by Molnar et al. (2017); Molnar et al. (2020); Molnar et al. (2018, 2019) and Khalil et al. (2020) perform rotational rifting experiments at lithospheric scale and examine the influence of inherited crustal and mantle heterogeneities. Despite propagating rifts towards the rotation axis, their models show occasionally lateral, shifts in rift localisation, perpendicular to the rift propagation direction. This may be attributed to the asymmetric opening of their setup. However, mantle and crustal heterogeneities primarily deflect rift structures and influence the rift pattern. Despite different scales and setups, first-order similarities such as a "v-shaped" extensional domain and a gradient in rift maturity decreasing towards the rotation axis, are common in these studies and our first-order observations fit well with the aforementioned studies.

In the following, we discuss similarities and differences between reference model and models with varying maximum extension velocities and crustal configuration and put our findings into the context of recent modelling studies addressing rotational rifting. Moreover, we discuss basin evolution and provide a characterisation of rift propagation in the light of fault localisation, fault segmentation and fault growth based on high-resolution 3D Stereo Digital Image Correlation.

5.1. The role of the viscous layer and its influence on inward migration of fault activity

Progressive inward migration of active faulting from initial large boundary faults to intra-rift faults leads to progressive narrowing of the
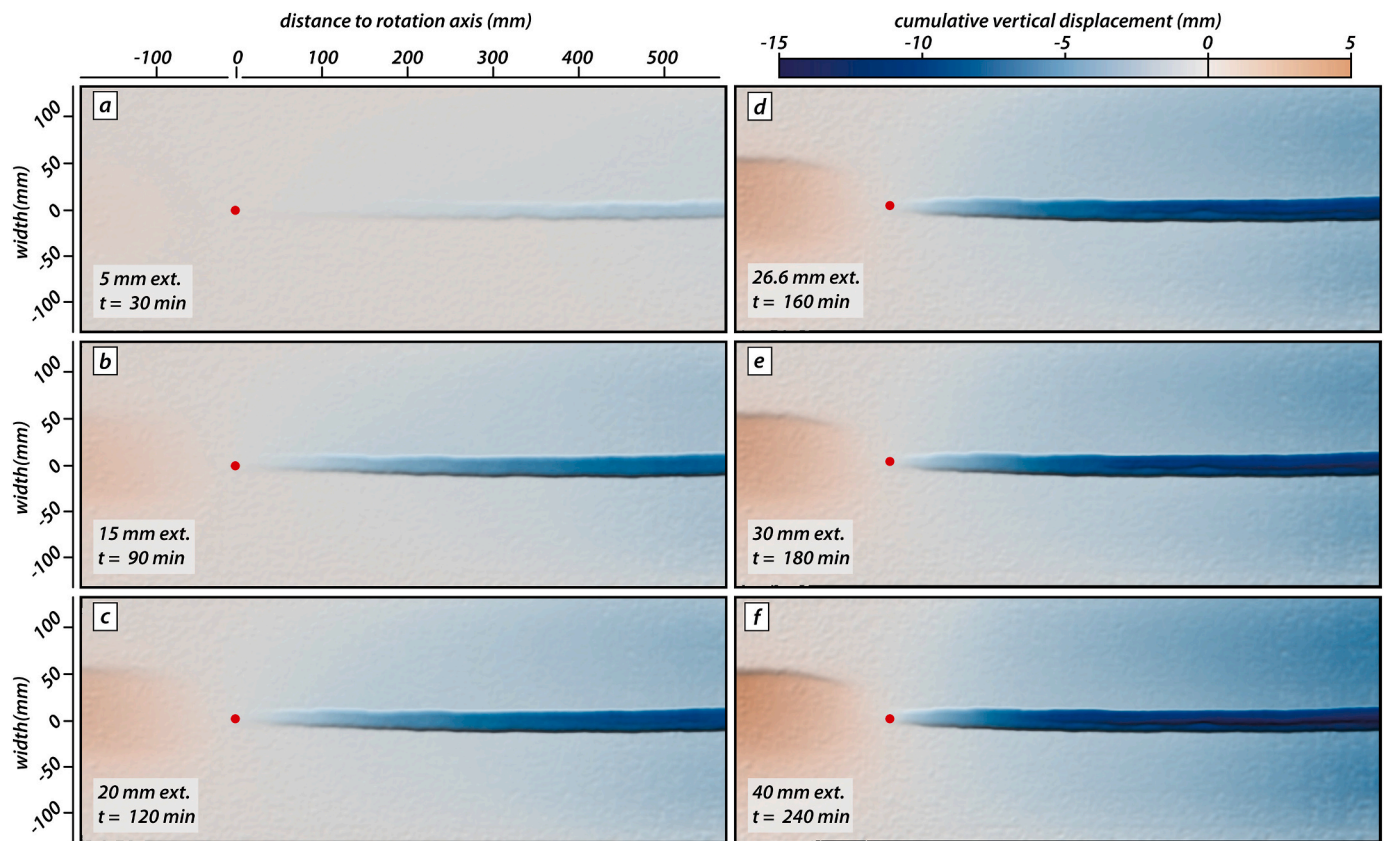
Fig. 8. Cumulative vertical displacement maps for different time steps. Red colours indicate an increase in topography in the compressional domain over time. Blue colours show subsidence in the extensional domain with a prominent rift basin, propagating towards the rotation axis (red dot).

tectonically active rift. This has not only been shown in quantitative modelling studies of orthogonal and oblique rifting (e.g., Agostini et al., 2009; Corti, 2012; Corti et al., 2013; Corti et al., 2010) but is also observed in modelling studies investigating rotational systems (e.g., Molnar et al., 2017; Mondy et al., 2018; Zwaan et al., 2020).

For homogeneous models (i.e., no pre-existing weakness, inherited fabric, or weak seed), the average fault slip velocity and the number of faults in the brittle layer is governed by the stretching and simultaneous thinning of the underlying viscous layer due to the applied extension. The rate of thinning of the viscous layer decreases over time providing less vertical displacement and related accommodation space. Subsequently, fault slip along the marginal rift faults in the brittle layer decreases over time forcing the system to increase the number of faults by inward migration to accommodate bulk extension (Corti et al., 2010; Schueller et al., 2005). In Eq. (11), dh/dt is the thinning rate of a homogeneous viscous layer, A is the constant area (assuming mass conservation) of a 2D section with initial width w_0 and applied extension velocity v over a time t.

$$\frac{dh}{dt} = -\frac{A\,v}{(v\,t + w_0)^2} \qquad (11)$$

Thus, for higher divergence velocities, slip along rift boundary faults decreases faster as the viscous layer below thins faster, leading to an early inward migration of faulting activity in the brittle layer.

With respect to our models this would imply faster onset of rift narrowing and inward migration for a higher maximum divergence velocity. However, for models with higher divergence velocities, inward migration is progressively delayed (Fig. 11). This observation seems counterintuitive and is best seen in models with a brittle-ductile ratio $R_{BD} = 1$ (Fig. 11a). In contrast, for models with a higher brittle-ductile ratio $R_{BD} = 3$, deformation is taken up mostly by the rift boundary faults, regardless of the maximum divergence velocity. This relation

between brittle crust thickness and intra-rift faulting fits well with conclusions from previous studies (e.g., Corti et al., 2010).

CT imagery cross sections may give an answer for the observed delayed inward migration for higher maximum divergence velocities (Figs. 6i-l, 7c,d, Supplementary Figs. S3 and S4). Intra-rift faults first form as antithetic normal faults (with respect to the rift boundary faults) and subside due to displacement accumulating along the rift boundary faults (Fig. 6j, Supplementary Fig. S3). This phase coincides with the low strain rate values along the intra-rift faults (Fig. 10b). It is only after the rift boundary faults laterally move apart that intra-rift faults reach the brittle-ductile interface. At this point, fault activity increases along intra-rift faults and drops along rift boundary faults (Figs. 6k and 10c). Corti et al. (2010) propose a localised zone of high shear stress at the brittle-ductile interface, where brittle strength is low and faulting initiates (i.e., above the seed location). In that sense, intra-rift faults in our models become active (i.e., rift inward migration) when they reach the zone of high shear stress at the brittle-ductile interface and fault activity along rift boundary faults ceases.

We assume that this process is related to localised upward flow of the viscous material in the seed region (see e.g., Zwaan et al., 2017; Figs. 6k, l 7c) which shifts the brittle-ductile interface upwards. With progressive upward shift, the formerly scarcely (if any) active intra-rift faults are in proximity of the high shear stress zone and start to accommodate displacement. With higher divergence velocities (e.g., Mod_1_20, Mod_1_40), upward flow in the viscous layer along the weak seed may not proportionally increase. Consequently, intra-rift faults remain for a longer period outside of the high shear stress zone allowing the rift boundary faults to accommodate further displacement. Note that the suggested mechanism may provide an explanation for the delay in inward migration, however, further work investigating the cause of this phenomenon is needed.
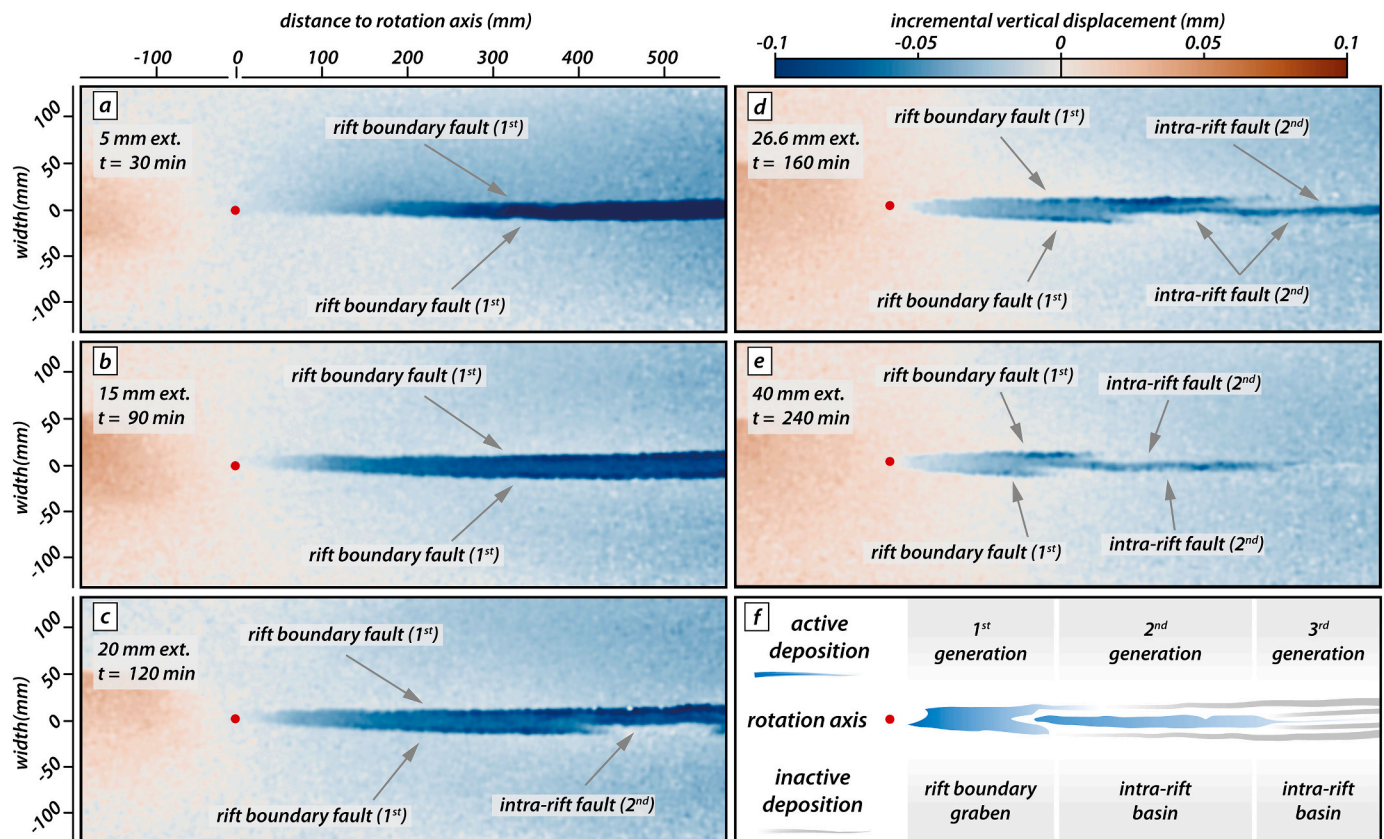
Fig. 9. Incremental vertical displacement maps for different time steps. a-e) Evolution of active subsidence as the rift propagates towards the rotation axis (red dot). Subsidence in the first 90 min is defined by a pair of conjugate rift boundary faults. The activation of intra-rift faults is segmented and leads to stepwise narrowing of active subsidence. f) Interpretation of the active subsidence arrangement at the final model stage. Blue colours indicate zones of active subsidence.

5.2. Rift morphology and basin symmetry

We document the control of active tectonics on basin subsidence and rift geometry by combining incremental vertical displacement maps with topographic surface profiles. Incremental displacements may focus active deformation on either a set of conjugate faults at the time or on faults belonging to two different fault generations. Hence, we define phases of symmetric and asymmetric distribution of active deformation (as seen in cross-sections perpendicular to the rift axis), respectively. The morphological evolution is similar in all nine conducted experiments and incremental vertical displacement patterns strongly coincide with incremental strain rate maps (Fig. 12). We therefore return to our reference model Mod_1_10 to investigate rift morphology. Analogous to the rift inward migration, we discuss displacement distribution and its influence on rift morphology and subsidence as a function of i) the distance to the rotation axis and ii) time.

i) Distance to the rotation axis

As illustrated in our models, inward migration of fault activity occurs in segments with rift boundary faults forming first, followed by subsequent generations of intra rift faults with increasing bulk extension in the respective rift segment (Figs. 10, 11 and 12). In rift transects at different distances from the rotation axis, inward fault migration occurs asynchronously along both intra rift conjugate faults (Fig. 12). Therefore, faults belonging to two different fault generations are locally active at the same time. For example, in section P2 in Fig. 12a, one side of the rift boundary fault is still active (BF 1st in section P2, Fig. 12a), while fault activity on the opposite rift flank has migrated inwards (IF 2nd in section P2, Fig. 12a). This results in asymmetric distribution of deformation due to the phased switching and strain partitioning between

boundary and intra rift faults (see profile P2, Fig. 12a). We call such a transient rift stage hereafter the asymmetric rifting stage.

While in the distal rift segment (profile P2, Fig. 12a) two active fault generations cause asymmetric deformation distribution, at the same time and closer to the rotation axis deformation distribution is symmetric resulting in a symmetric rift morphology at this stage. In this proximal domain of the rift (profile lines P5 and P6, Fig. 12a), fault activity is located at the conjugate rift boundary faults resulting in symmetric subsidence. Similarly, to the asymmetric rift stage, we call this stage hereafter the symmetric rifting stage.

ii) Time

With progressive rift extension (e.g., time; compare Fig. 12a and b, and Fig. 12b and c), previously symmetric rift domains (i.e., profile line P5, Fig. 12a) become asymmetric and vice versa (i.e., profile line P2, Fig. 12a). At profile line P2 in Fig. 12b, faulting is mainly focused on the intra rift faults which controls a localised symmetric deformation distribution. Bends in the topographic profile in P2 in Fig. 12b on both sides of the rift reflect the completed inward migration and therefore, the transition from asymmetric to symmetric rifting stage. In contrast, at profile line P5 in Fig. 12b, deformation distribution is asymmetric. The local activation of different fault generations is a function of bulk extension on this respective transect. For profile lines P2, P5 and P6 bulk extension values increase between 120 and 240 min by 4.5%, 2.5% and 2%, respectively. All three transects consistently experience switches between symmetric and asymmetric phases of deformation distribution for distinct bulk extension values.

In summary, for each fault generation localisation and displacement transfer between faults is expressed by symmetric and asymmetric rift stages. During the model runs, different rift segments along the rift axis
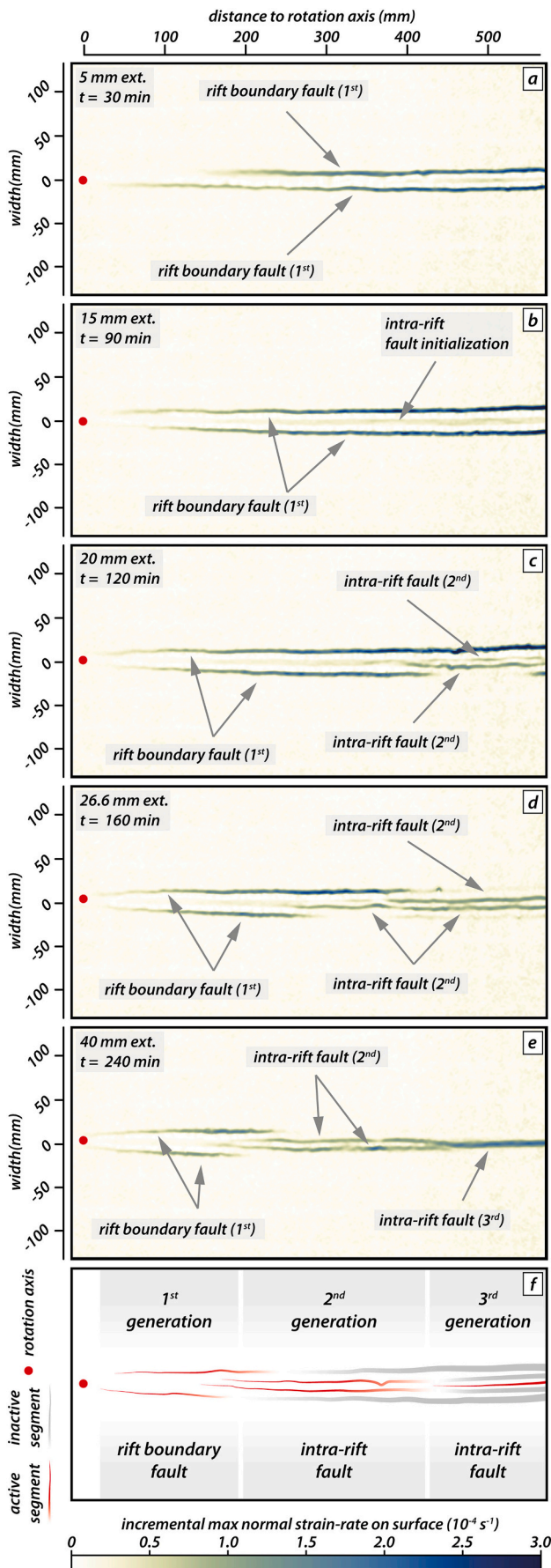
Fig. 10. Incremental strain rate maps for different time steps. a-e) Incremental strain rates reveal a segmented fault activity along continuous fault planes. f) Different fault generations are activated simultaneously but at different positions along the rift axis. Maximum normal strain rate refers to Eq. (10) divided by Δt = 60s.

experience inward migration of fault activity at different time steps (different extension values). This complies with the deformation distribution. In segments of ongoing inward rift migration, deformation distribution is asymmetric. In contrast, rift segments show symmetric deformation distribution, where conjugate faults of the same generation are active.

5.3. Styles of fault growth controlling rift propagation

As a measure of displacement along faults, vertical displacement is referred to as throw and is commonly measured in field studies, where true displacement is poorly preserved (e.g., Cartwright et al., 1995; Jackson et al., 2017; Jackson and Rotevatn, 2013; Walsh et al., 2003). Plotting displacement against along-strike fault distance yields typical displacement/length relationships. Moreover, studies using analogue experiments have investigated fault growth (e.g., Bellahsen et al., 2003a; Schlagenhauf et al., 2008) giving insights into fault segmentation and linkage processes. For practical reasons, we use cumulative maximum normal strain (instead of displacement; Eq. (10)) as a proxy for fault activity and demonstrate, based on our reference model Mod_1_10, the necessity of high temporal resolution image series to unravel early stages of rift propagation in rotational settings.

5.3.1. A switch in fault growth mechanism

Strain maps of cumulative maximum normal strain show two distinct growth phases of the rift boundary faults with a first phase of rapid bidirectional lengthening followed by slow and unidirectional propagation towards the rotation axis. We demonstrate the rapid switch in fault growth mechanism based on early stages at around 1.5% of bulk extension for model Mod_1_10 (Fig. 13). There, well-developed continuous, as well as isolated segments of conjugate boundary faults show high total strain separated by zones of lower total strain (Fig. 13a). Boundary fault F1 is a continuous fault whereas the conjugate boundary fault F2 still consists of isolated segments. The single discrete fault segments of F2 merge within two minutes into a continuous boundary fault segment (Fig. 13c,e). When plotting cumulative strain along the fault length, fault segment linkage is indicated by strain minima along the profile and is also visible for linkage events prior to this event (e.g., for F2 at a distance 450 mm to the rotation axis; Fig. 13b,d,e). Note that the linkage of individual segments occurs by bidirectional growth. That is, faults also grow oppositely with respect to the rift propagation direction.

In all our models, early rift propagation is dominated by bidirectional growth of fault segments towards and away from the rotation pole shortly before switching fault growth mechanism (see also Fig. 15 and Section 5.3.3). Subsequent growth of linked faults occurs unidirectionally towards the rotation axis. While boundary fault F2 still grows step-wise by segment linkage (indicated by strain minima in between segments; Fig. 13b,d,f), F1 advances to a linear growth mechanism indicated by linearly decreasing strain values towards the rotation axis (Fig. 13 b,d,f). After less than 25% of total bulk extension, all isolated fault segments have been linked to two distinct, continuous, and conjugate rift boundary faults and fault growth has switched to linear, unidirectional growth towards the rotation axis.

5.3.2. Strain partitioning between competing conjugate faults

The switch in fault growth mechanism has a distinct effect on the overall rift propagation (Fig. 14). Stepwise fault growth due to segment linkage occurs in early stages resulting in high fault tip propagation rates
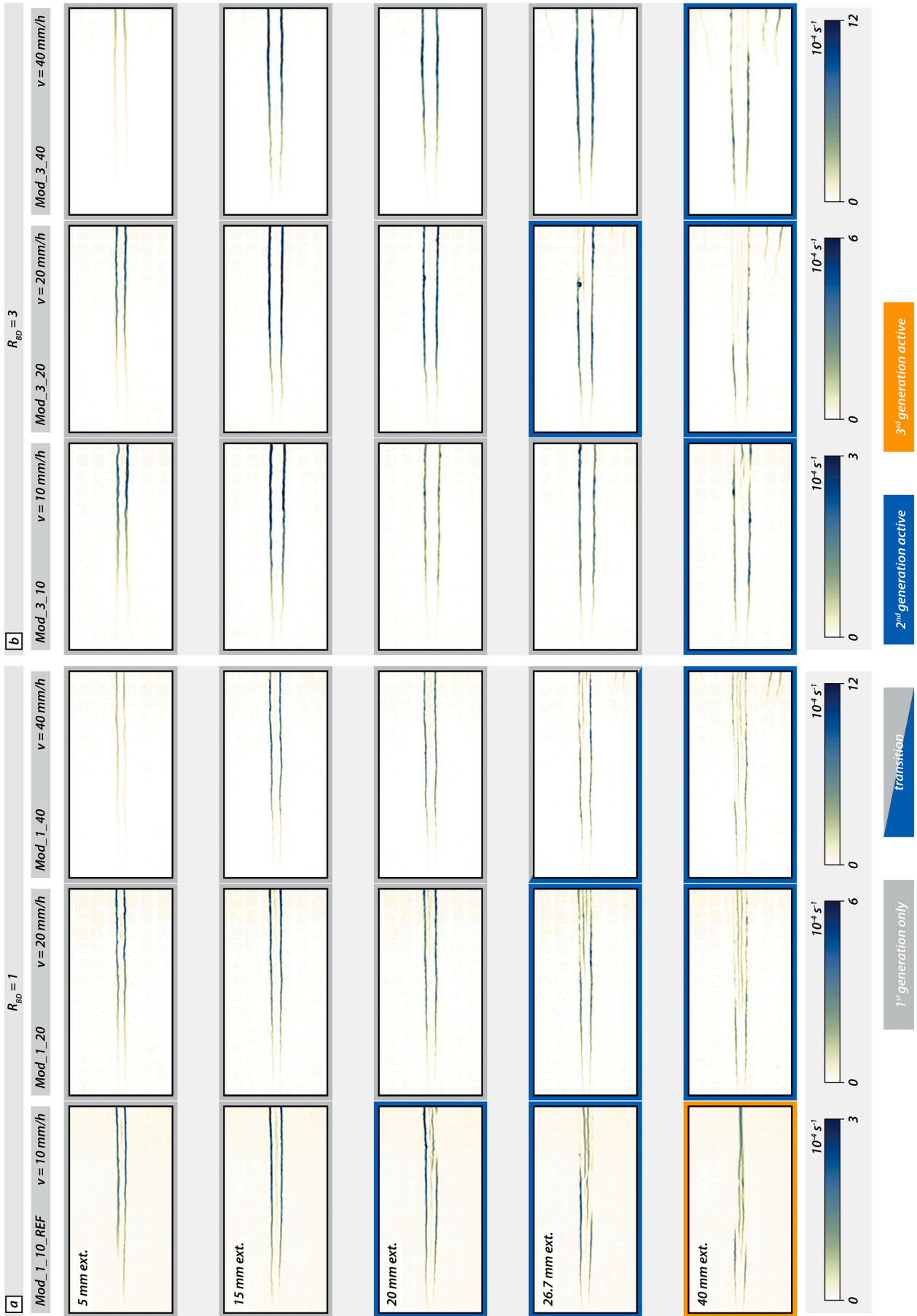
(caption on next page)

Fig. 11. Strain rate maps for models with varying maximum divergence velocities and different brittle-ductile ratios. a) Effect of increasing maximum divergence velocity for models with $R_{BD} = 1$; inward migration of faulting activity is successively retarded for higher divergence velocities. b) Models with $R_{BD} = 3$; as a geometrical consequence of the thicker brittle layer, inward migration occurs at a later stage, relative to models with $R_{BD} = 1$. Frame colours indicate the number of active fault generations. Note the different scale for the colour bars.

(Fig. 14b). Eventually, when both boundary faults reach the unidirectional, linear growth stage propagation rates drastically drop (Fig. 14b). Fig. 14c shows the position of the conjugate boundary fault tips over time. Steep slope segments within the first hour, indicate fast growth by linkage of fault segments (incline in Fig. 14c, d). Rapid rift propagation is followed by a long period, in which boundary fault tips propagate less effectively (plateau in Fig. 14c,d). During the rapid growth phase, the curves of both boundary faults show steeper segments alternating with plateaus indicating periods of minor fault growth. This characteristic pattern of fault tip advance is well demonstrated in the 30 to 40 min interval (Fig. 14c inset). During this time interval, the fault tip position of rift boundary fault F1 has experienced intermittent phases of fast growth (steep slope) and less prominent growth (less steep slope). The onset of flattening coincides with the onset of a linear growth stage of boundary fault F2. The contrasting growth rates of the two conjugate boundary faults reflect strain partitioning. When growth of one boundary fault is favoured, growth of the other is temporarily suppressed and vice versa. The bulk extension across the rift zone is mostly accommodated by one fault at the time. This explains the two different, simultaneously active growth mechanisms in Figs. 13 and 14. Growth rates of boundary fault F1 are highest during early fault localisation with a maximum growth rate of 4.8 m per hour at times when growth of F2 is inactive (Fig. 14d). Only shortly after activity of boundary fault F1 decreased, growth rates for F2 rise to peak rates of about 3 m per hour (Fig. 14d). In contrast to F1, peak growth rates for F2 are smaller. However, rapid changes in fault growth rates of F1 allow F2 to maintain growth rates above average for a longer period to keep up with the rift tip position of F1. Only after one boundary fault has reached linear growth stage, ongoing bulk extension is localised on the other boundary fault to complete the linkage stage and reach linear growth. In contrast to inward migration of fault activity, strain partitioning between competing conjugate faults occurs at much smaller time scales and no evident influence on the rift morphology (i.e., a change from symmetric to asymmetric displacement distribution) is observed in surface view.

5.3.3. Conceptual fault growth model

We have shown that rift growth by segment linkage represents an effective way of accommodating high extensional strain in the distal rift zone far away from the rotation axis. Consequently, it yields high mean rift propagation rates which then drastically decrease and stabilize as the growth mechanism changes to linear unidirectional growth. The switch in fault growth mechanism holds for all nine analysed experiments (Fig. 15). Notably, all models show a distinct change of growth mechanism at around 25% of the total bulk extension, which also reflects a change in the rift propagation rate (Fig. 15a). Based on the two distinctive growth phases, 75% of the total rift length in our models establish within the first 25% of the model run time (see orange arrows and green arrows in Fig. 15a). The early lengthening of boundary faults is also reflected in the relationship between fault length and accumulated strain (as a proxy for displacement; Fig. 15b). The fault behaviour through time is characterised by a phase of dominant fault lengthening and little strain accumulation (orange arrows), prior to a second phase of dominant strain accumulation and minor lengthening (purple arrows). During the first phase 75% of the total fault length is established and strain accumulation mainly occurs in concert with the last 25% of fault lengthening. The first phase of fault lengthening in Fig. 15b reflects the first phase of rapid rift propagation in Fig. 15a. Consequently, the phase of major strain accumulation (purple arrows Fig. 15b) reveals that the second phase of rift propagation is in concert with a dominant phase of strain accumulation. In accordance with Figs. 13 and 14, Fig. 15c, shows

that distal segments relative to the rotation axis accumulate strain along linking fault segments enabling the rift to propagate rapidly over 75% of the total length within 25% of the applied bulk extension (orange arrows Fig. 15a-c). Proximal segments relative to the rotation axis experience less bulk extension and grow linearly, expressed by slow rift propagation over the remaining 25% of length within the remaining 75% of bulk extension (green arrows Fig. 15a,c). Simultaneously to linear rift propagation near the rotation axis, distal segments accumulate further strain (purple arrows Fig. 15b,c).

To further discuss fault growth of boundary faults in our models, we consider two common conceptual fault growth models. In the "propagating fault model", fault displacement and length increase synchronously by fault linkage (as expressed by displacement minima along strike of normal faults) and fault tip propagation (see Rotevatn et al., 2019 and references therein; Walsh and Watterson, 1988; Watterson, 1986). In contrast, the "constant length model" states that faults establish their length almost instantaneously followed by continuous increase of displacement (Nicol et al., 2005; Walsh et al., 2002). Although these two conceptual models were designed to explain fault growth under orthogonal extension, we compare them with fault growth in our rotational extension models. We document an early phase of rapid fault growth by fault segment linkage (see Figs. 13, 14 and 15). This is expressed by the occurrence of displacement minima along strike, an observation typically attributed to the propagating fault model. As a result, the rift tip rapidly propagates towards the rotation axis and establishes a greater part of the final rift length at an early stage. Fault segment linkage together with almost instantaneous lengthening seems to be a conflicting observation favouring neither of the two conceptual models. In addition, all our models include linear weak "seeds" to localise deformation. The local weakening of the brittle strength is similar to a pre-existing crustal fabric and would favour the constant length model (e.g., Morley, 1999; Nicol et al., 2005). Nevertheless, we document rapid lengthening (constant length model) which, itself relies on fault segment linkage (fault propagation model). To solve this discrepancy, Jackson et al. (2017) proposed that propagating and constant length model mutually, rather than exclusively, contribute to the fault development with a very early phase of growth of small segments that increase in length and displacement before they link to form a larger structure. This very early stage may have remained unresolved in nature due to relative low temporal resolution. Indeed, Rotevatn et al. (2019) describe data which behaves broadly according to the constant length model and report an initial stage with phases of significant displacement accumulation rather than lengthening (Fig. 16c). We also document such early stages of strain accumulation within data that overall behaves according to the constant length model. Short impulses of growth may not just only reflect strain partitioning between conjugate boundary faults (Fig. 14c inset) but may also be indicative for early stages of strain accumulation within the overall phase of fault lengthening.

The two distinct fault growth mechanisms documented in our models thus mutually contribute to fault growth (and ultimately rift propagation) and represent transient stages of a complex evolution. This refers to the concept of a hybrid growth model (Rotevatn et al., 2019), in which rapid fault lengthening itself is enabled by fault segment linkage followed by a second phase dominated by strain accumulation. Note that in our models, unidirectional growth during the second phase is dictated by the gradient of the applied bulk extension along the rift axis. This is in strong contrast to orthogonal extension where lateral fault propagation is generally inferred to occur bidirectionally (Jackson et al., 2017).
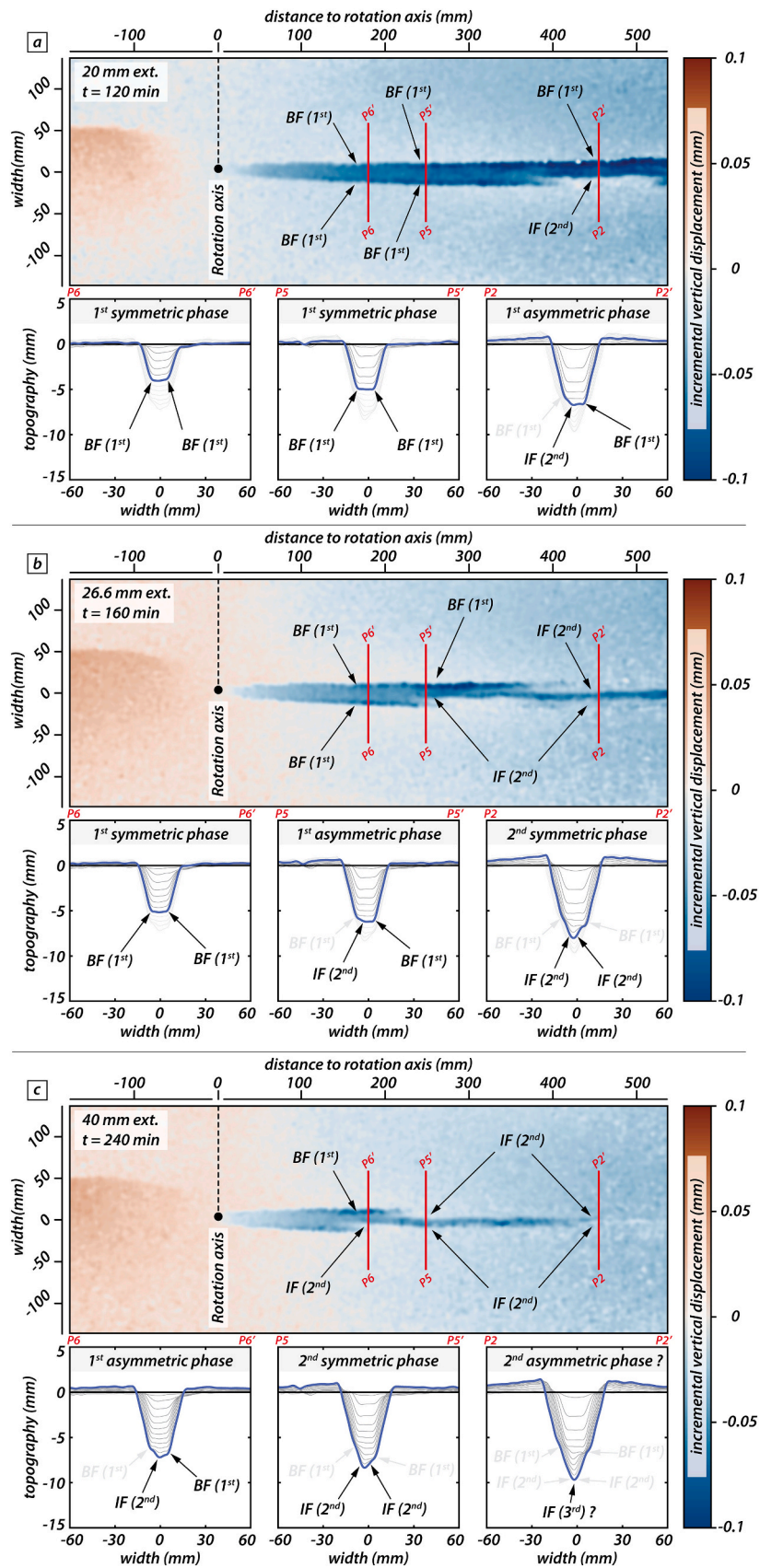
Fig. 12. Incremental vertical displacement maps and topographic profile lines at 120 (a), 160 (b) and 240 min (c). Topographic profile lines show cumulative vertical displacement at positions of the red profile lines in the incremental vertical displacement maps. Bold blue line indicates topography at the actual time step.
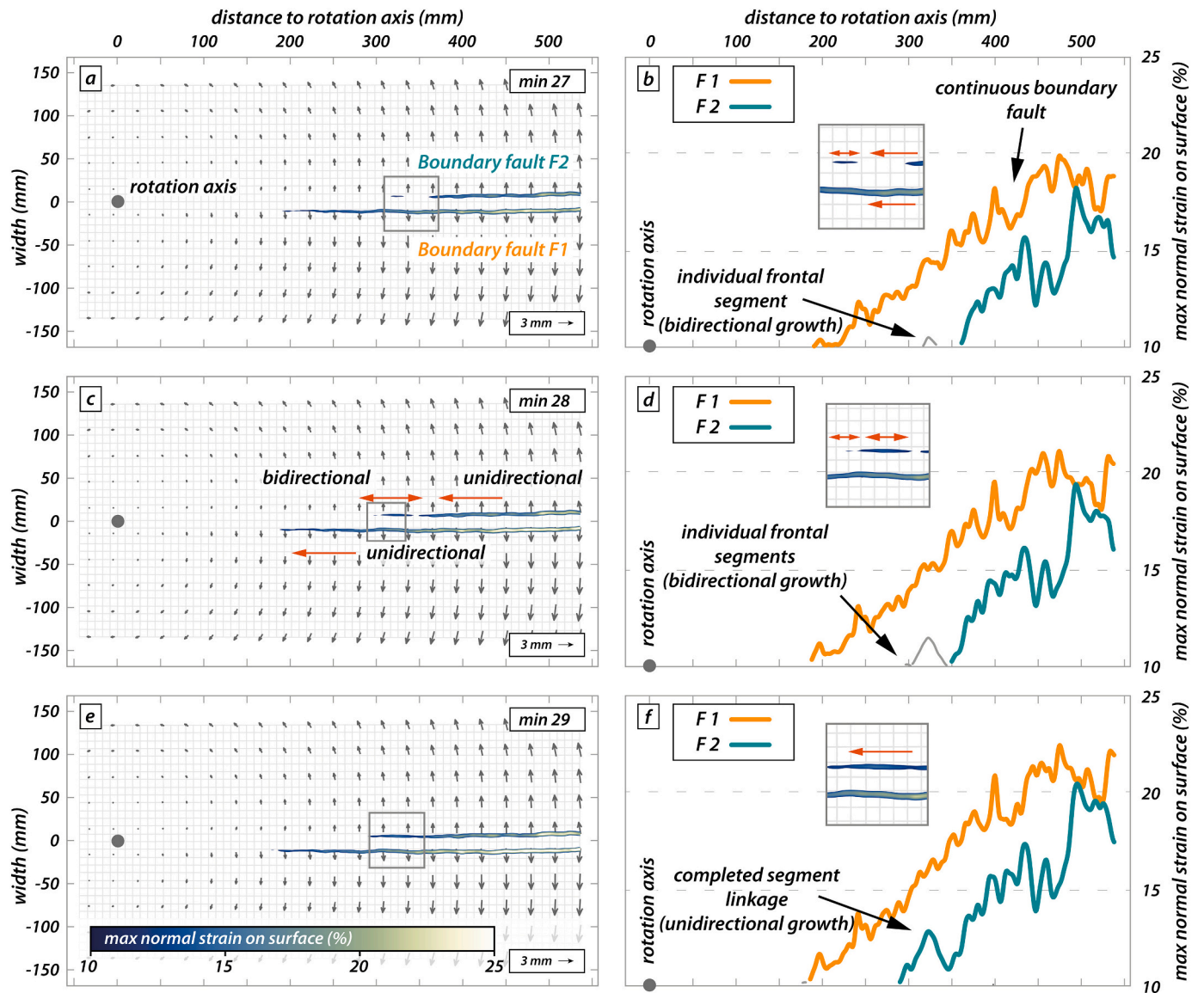
Fig. 13. Top views (a, c & e) and corresponding line plots (b, d & f) of total normal strain evolution along rift boundary faults between minutes 27 and 29. Boundary fault F2 grows by linking former individual segments. Boundary fault F1 acumulates strain along formerly linked segments (from pos. 550 mm to 300 mm) while further growth happens by linear unidirectional growth (300 mm – 100 mm). Small grey lines indicate segments which develop but have not yet been connected with the main boundary fault (b, d & f). Grey solid dot indicates rotation axis.

5.4. Implications for nature and potential predictions

The Taupo Rift Zone (Fig. 1) is characterised by a gradient in rift maturity along the rift axis and changes in deformation style along the rift axis (Villamor and Berryman, 2006). Its southward propagation and the changes in extension rates along the rift axis have been a matter of debate (Beanland and Haines, 1998; Villamor and Berryman, 2006; Wallace et al., 2004) but GPS data and field evidence are in favour of a rotational opening of the Taupo rift due to a clockwise rotation of the North Island of New Zealand (Nicol and Wallace, 2007; Wallace et al., 2005). Models suggest that tectonic block rotation arises from the change of subduction of the Pacific plate along the Hikurangi Trough, to a collision of the Hikurangi Plateau and Chatham Rise further to the south (Wallace et al., 2004). Extension rates along the rift axis range from about 17 mm/a to 2 mm/a in the northern and southern segments, respectively and block rotation rates are in the order of $3° - 3.5°/Ma$ over the last 1.5 Ma (Nicol and Wallace, 2007). These values fit well for our high-divergence velocity models and are still comparable to our low divergence velocity models. Although nature depicts a more complex rift

evolution, we consider the Taupo rift to be an excellence natural example of rotational rifting to discuss the implication of our models for nature.

Villamor and Berryman (2006) conclude, based on gravitational anomalies, that extension rates along the Taupo Rift change abruptly along distinct accommodation zones (parallel sided) rather than gradually (wedge shaped; Beanland and Haines, 1998). These sharp gradients are also expressed in the shape of different rift segments active at different times (i.e., old, young, and modern Taupo Rift; Fig. 1). Stepwise migration of fault activity towards the rift axis indeed is enticing and favourable for the parallel sided extension model (Villamor and Berryman, 2006; Villamor et al., 2017). However, our models show that even in the presence of a constant divergence velocity gradient, inward migration of fault activity does occur stepwise and no abrupt changes in extension rates are needed (Fig. 10). In that light, the gradual decrease in the extension rates towards the southern end of the Taupo Rift (Nicol and Wallace, 2007) does not contradict the stepwise migration but can all the more explain the overall shape of the Taupo rift. The active modern Taupo rift (0–25 ka) consists of a 40 km and 15 km wide zone in
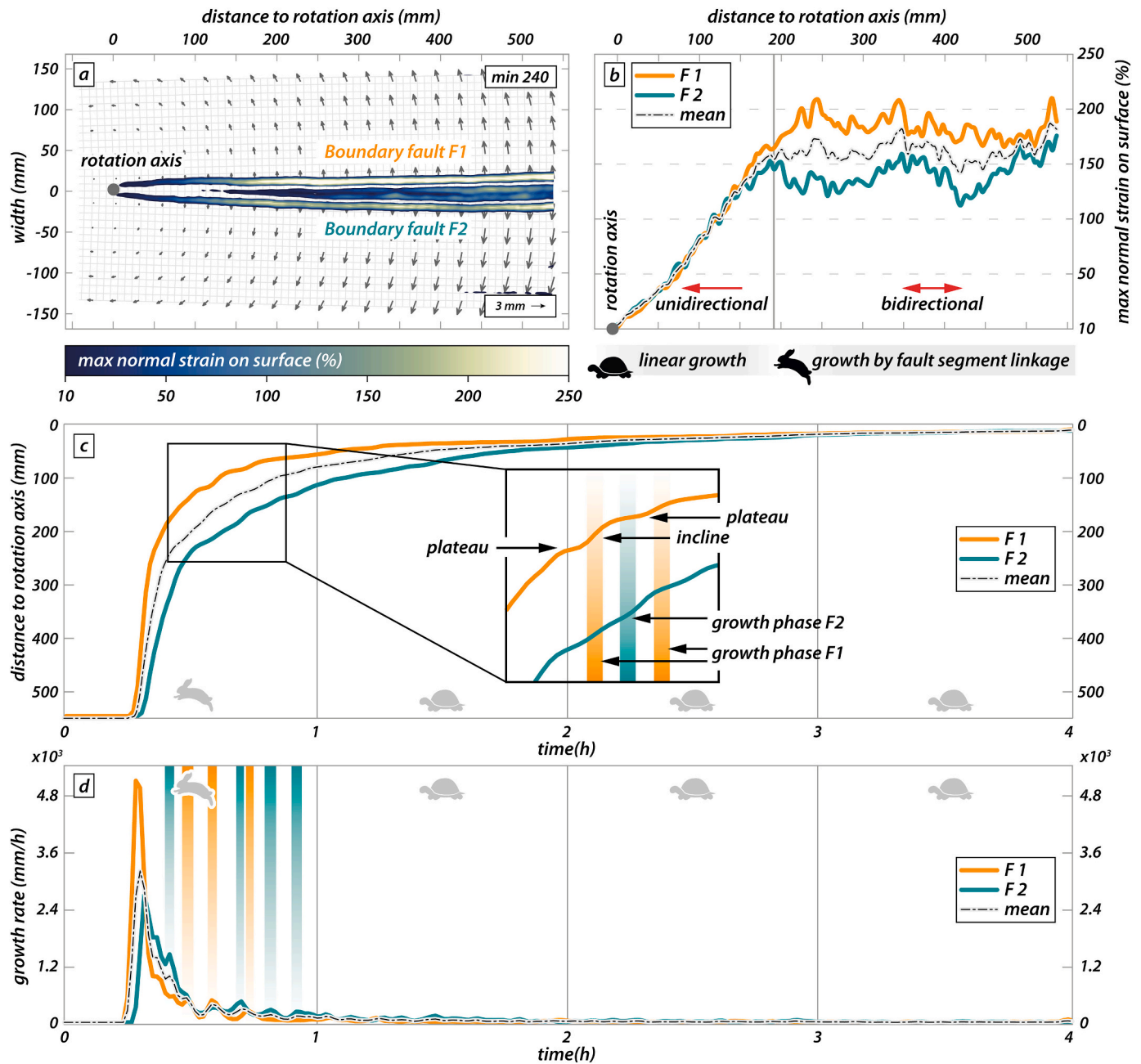
Fig. 14. Final stage of strain evolution along rift boundary faults. a) Both boundary faults reach a terminal position near the rotation axis. b) The conjugate boundary faults show a characteristic change in strain accumulation at distance to rotation axis = 200 mm with a change from bidirectional fault linkage to unidirectional linear growth. c) Fault tip position for both boundary faults over the entire model runtime show rapid growth within the first hour followed by a phase of slow growth. d) Growth rates for both boundary faults over the entire model runtime. Phases of growth of one fault loosely coincide with phases of stagnation of the other fault showing a anticyclic growth due to strain partitioning within the first hour of the model run.

the Southern and Northern part of the Taupo rift, respectively (e.g., Villamor et al., 2017). Although nature depicts a more complex evolution including magmatic processes, incremental strain rate analysis of our analogue models show patterns where multiple generations of faults are active at the same time along the rift axis (Figs. 10 and 11). The wider area of fault activity close to the rotation axis in our models (Fig. 10e) is comparable with the southern Taupo Rift and provides a potential explanation for step wise widening of the active fault zone towards the present-day termination of the Taupo rift (also compare Fig. 8 in (Villamor et al., 2017) and Fig. 10 in this study).

Fault growth in our models depicts a detailed evolution of rift boundary fault growth and partitioning of displacement between competing conjugate faults (Section 5.3; Figs. 14 and 17). We show that a switch in growth mechanism from segment linkage-dominated to unilateral propagation occurs only after a short time (20–25%) of the model run. In the context of the Taupo Rift, this means significant increases of fault maturity within a range of 300 ka (Nicol et al., 2010). However, assessing early stages of fault growth poses a fundamentally difficult task since displacement-length ratios recorded from recent and ancient rifts only represent static snap shots of a kinematically more complex fault growth evolution. Techniques such as back stripping (e.g., Jackson et al., 2017) may improve the understanding of normal fault growth in nature. However, in the case of basin underfilling, analysis of growth strata becomes problematic (Rotevatn et al., 2019). Therefore, in
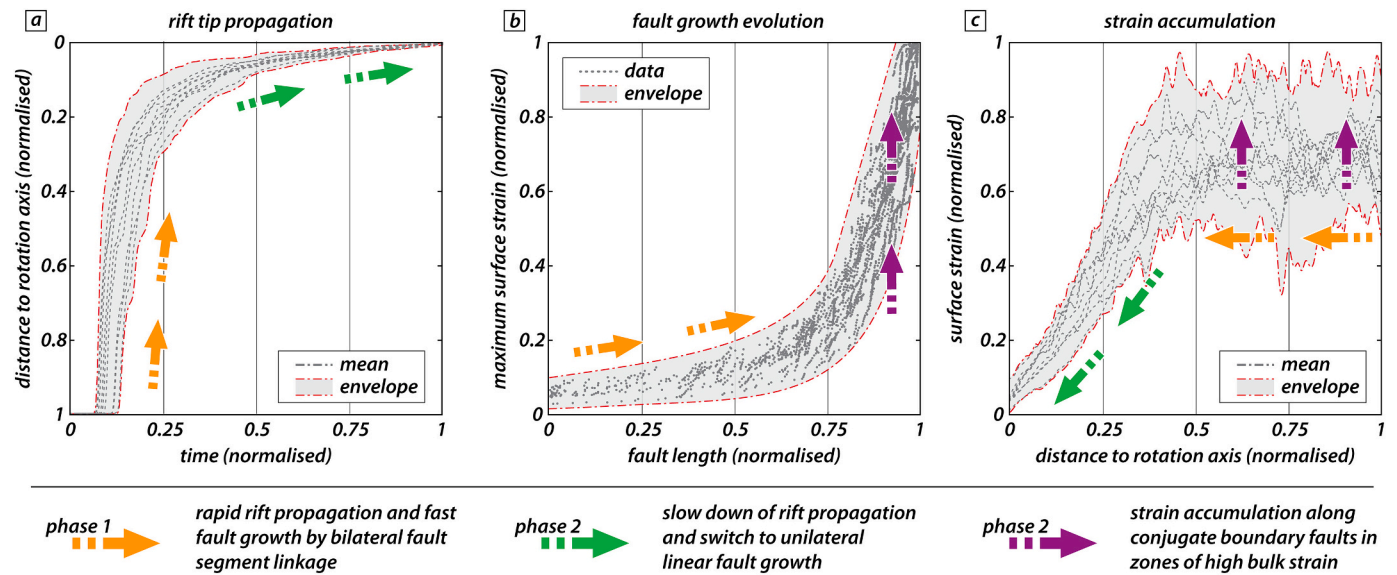
Fig. 15. Compilation of rift propagation and fault growth for all nine models a) rift tip propagation shows a short initial phase of rapid propagation (orange arrows) followed by slow propagation over a longer time (green arrows). X-axis and y-axis denote normalised model run time and normalised rift length, respectively. b) Normalised fault length vs. normalised maximum surface strain for automatically tracked fault segments. An early phase of fault lengthening (orange arrows) is followed by strain accumulation and minor lengthening (purple arrows) c) Normalised fault length vs. normalised surface strain. Strain accumulation along fault strike shows an early phase of rapid fault lengthening (orange arrows) followed by a phase in which rift boundary faults linearly grow towards the rotation axis (green arrows) and established fault segments accumulate further strain (purple arrows). Note that arrow colours in a,b and c indicate the identical stage of fault growth and rift propagation.
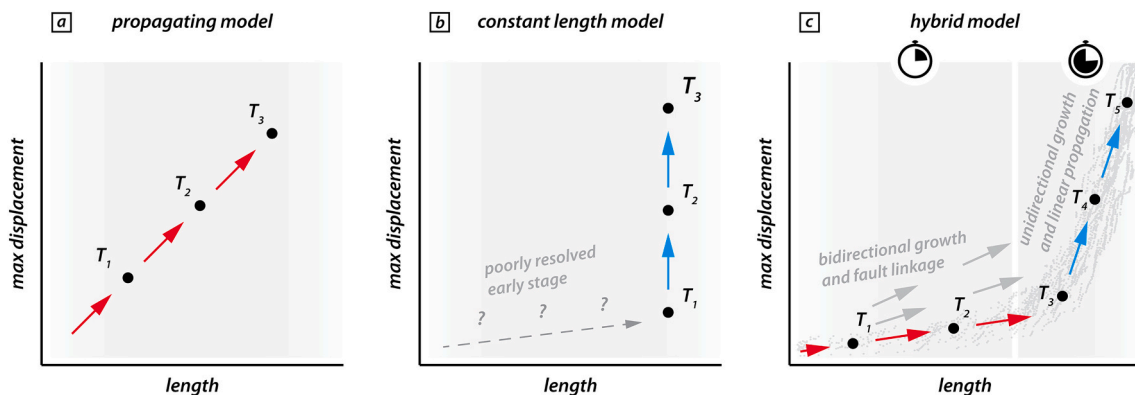

Fig. 16. Recent conceptual fault growth models. a) propagating model with incremental fault lengthening in concert with displacement accrue (Walsh and Watterson, 1988; Watterson, 1986). b) constant length model with almost instantaneous establishing of fault length, followed by displacement accumulation of under displaced faults (Walsh et al., 2002). c) hybrid fault growth model proposed by Rotevatn et al. (2019). An initial stage of dominant fault lengthening is accompanied by sporadic displacement accrue, leading to various slopes of the lengthening phase. Fault lengthening at this early stage occurs by fault segment linkage, leading to rapid growth and apparent instantaneously established fault lengths. The second stage is dominated by displacement accumulation and minor fault lengthening. Light grey dots indicate data from this study. Note that the lengthening stage might occur at time scales which are rather poorly resolved in nature.
Modified after Rotevatn et al. (2019).

nature time constraints on fault activity are often rather poor and hence, such early stages of bidirectional lengthening and strain accruement as seen in our models are difficult to resolve, which highlights the importance of modelling studies on fault growth at high temporal resolution.

6. Conclusion

We performed a series of brittle-viscous analogue model experiments to gain insights into natural rifts that have formed under the influence of along strike extension gradients. Analysis of our models involved visualisation by X-ray computed tomography and quantification of surface deformation. The application of temporal high-resolution 3D stereo DIC allows a detailed quantitative analysis of fault growth revealing fault linkage and fault propagation mechanisms that have not been

recognized before. Our results are summarized below and have important implications for conceptual models of fault growth.

- Initial bulk extension during the first phase is accommodated by a set of conjugate normal faults above the viscous seed. These rift boundary faults initially dip at 70° and limit the rift basin.
- The fault growth evolution of the rift boundary faults is characterised by a first rapid phase of fault lengthening accompanied by minor displacement, followed by a second phase of pronounced displacement and minor fault lengthening towards the rotation axis.
- The first phase is characterised by bidirectional fault growth through the linkage of discrete fault segments which is an efficient mechanism for fault lengthening. This bidirectional fault growth can only be detected by applying high-temporal resolution DIC analysis.
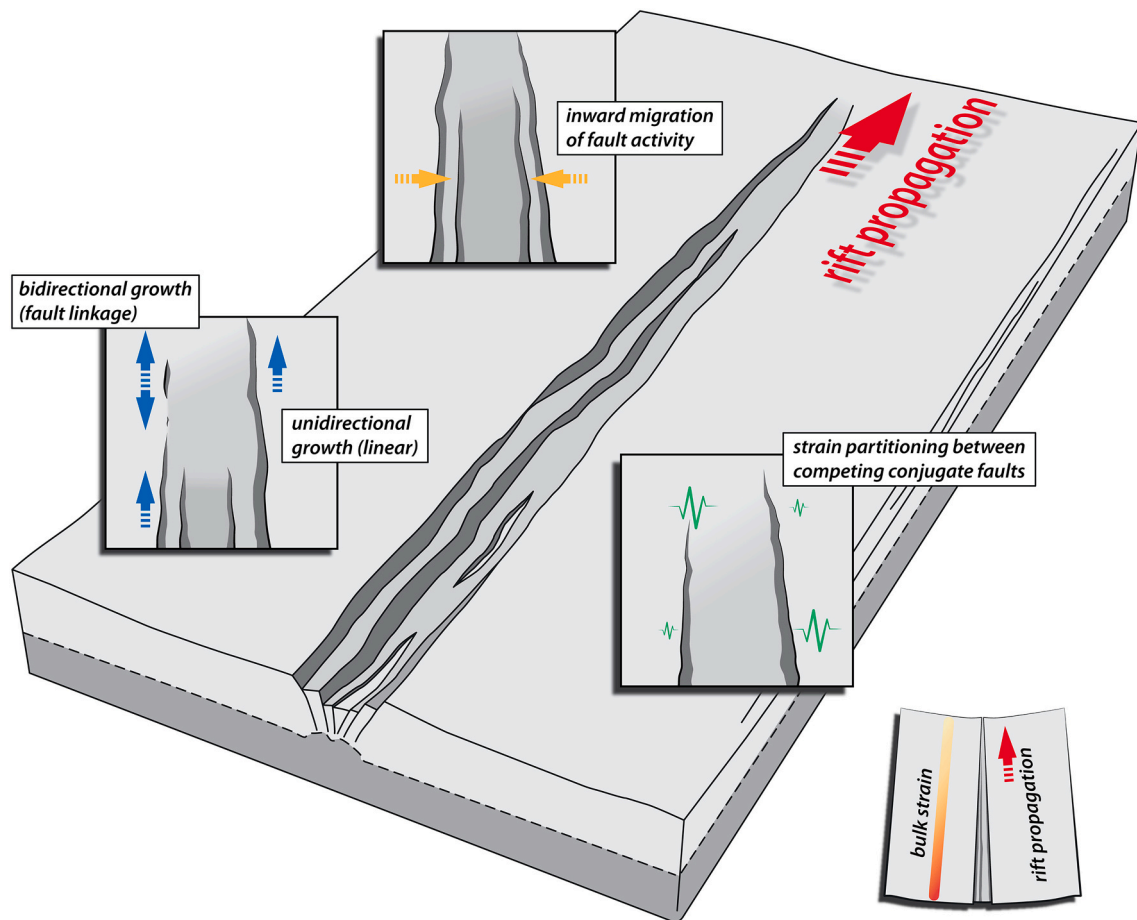
Fig. 17. Sketch showing key mechanism of rotational rifting in this study: Bidirectional vs. unidirectional growth, inward migration of fault activity and strain partitioning among competing pairs of conjugates.

- Fault tip propagation and fault displacement occurs alternatingly on one of the two rift boundary faults indicating strain partitioning between the conjugate faults: when one of the normal faults propagates laterally and accumulates displacement, the oppositely dipping normal fault shows little or no propagation and displacement, and vice versa.
- In contrast to the first phase of rapid fault lengthening by bidirectional fault growth, the second phase of minor fault lengthening occurs unidirectional towards the rotation axis.
- Intra-rift faults first form as anithetic normal faults and subside due to displacement accumulating along the rift boundary faults. With progressive applied bulk extension and rift widening, intra-rift faults reach the brittle-ductile interface and further strain accumulation is accommodated along intra-rift faults. The onset of such inward migration is segment-wise and asynchronous along the rift axis, initiating furthest away from the rotation axis and propagating towards it. This can result in segmented widening of fault activity towards the rift termination which is also observed in natural rift systems such as the Taupo Rift Zone.
- For models with higher maximum divergence velocities, inward migration of fault activity is delayed due to strengthening of the viscous layer (higher strain rates) which reduces viscous upward flow near the seed resulting in slower rotation of rift boundary faults and thus delaying formation of intra-rift faults.
- Fault growth evolution in our models is best described by a hybrid fault growth model. Although initially proposed for orthogonal divergence, this fault growth model, seems also to be valid for natural rifts where divergence velocities change along strike.

- Major fault lengthening in our models occurs rapidly. When scaled to nature, this implies that fault segment interactions leading to fault lengthening may be difficult to detect in natural rifts as time constraints on fault activity are often rather scarce. This emphasizes all the more the necessity of modelling studies to understand fault growth and, ultimately, rift propagation.

Data availability

Rheological measurements of the brittle materials used in this study are available in the form of two open access data publications via GFZ Data Services (Schmid et al., 2020a,b, respectively). An additional open access data publication on the GFZ Data Service (Schmid et al., 2021) provides additional images and movies of our models. Links to these datasets are provided in the reference list.

Declaration of Competing Interest

None.

Appendix A. Supplementary data

Supplementary data to this article can be found online at https://doi.org/10.1016/j.tecto.2021.229174.

References

Adam, J., Urai, J., Wieneke, B., Oncken, O., Pfeiffer, K., Kukowski, N., Lohrmann, J., Hoth, S., Van Der Zee, W., Schmatz, J., 2005. Shear localisation and strain distribution during tectonic faulting—new insights from granular-flow experiments and high-resolution optical image correlation techniques. J. Struct. Geol. 27, 283–301. https://doi.org/10.1016/j.jsg.2004.08.008.

Adam, J., Klinkmüller, M., Schreurs, G., Wieneke, B., 2013. Quantitative 3D strain analysis in analogue experiments simulating tectonic deformation: integration of X-ray computed tomography and digital volume correlation techniques. J. Struct. Geol. 55, 127–149. https://doi.org/10.1016/j.jsg.2013.07.011.

Agostini, A., Corti, G., Zeoli, A., Mulugeta, G., 2009. Evolution, pattern, and partitioning of deformation during oblique continental rifting: Inferences from lithospheric-scale centrifuge models. Geochem. Geophys. Geosyst. 10. https://doi.org/10.1029/2009GC002676.

Allken, V., Huismans, R.S., Thieulot, C., 2011. Three-dimensional numerical modeling of upper crustal extensional systems. J. Geophys. Res. 116. https://doi.org/10.1029/2011JB008319.

Allken, V., Huismans, R.S., Thieulot, C., 2012. Factors controlling the mode of rift interaction in brittle-ductile coupled systems: a 3D numerical study. Geochem. Geophys. Geosyst. 13. https://doi.org/10.1029/2012GC004077.

Beanland, S., Haines, J., 1998. The kinematics of active deformation in the North Island, New Zealand, determined from geological strain rates. N. Z. J. Geol. Geophys. 41, 311–323. https://doi.org/10.1080/00288306.1998.9514813.

Bellahsen, N., Daniel, J.M., 2005. Fault reactivation control on normal fault growth: an experimental study. J. Struct. Geol. 27, 769–780. https://doi.org/10.1016/j.jsg.2004.12.003.

Bellahsen, N., Daniel, J.-M., Bollinger, L., Burov, E., 2003a. Influence of viscous layers on the growth of normal faults: insights from experimental and numerical models. J. Struct. Geol. 25, 1471–1485. https://doi.org/10.1016/S0191-8141(02)00185-2.

Bellahsen, N., Faccenna, C., Funiciello, F., Daniel, J., Jolivet, L., 2003b. Why did Arabia separate from Africa? Insights from 3-D laboratory experiments. Earth Planet. Sci. Lett. 216, 365–381. https://doi.org/10.1016/S0012-821X(03)00516-8.

Benes, V., Scott, S.D., 1996. Oblique rifting in the Havre Trough and its propagation into the continental margin of New Zealand: comparison with analogue experiments. Mar. Geophys. Res. 18, 189–201. https://doi.org/10.1007/bf00286077.

Bonatti, E., 1985. Punctiform initiation of seafloor spreading in the Red Sea during transition from a continental to an oceanic rift. Nature 316, 33–37. https://doi.org/10.1038/316033a0.

Boutelier, D., 2016. TecPIV—a MATLAB-based application for PIV-analysis of experimental tectonics. Comput. Geosci. 89, 186–199. https://doi.org/10.1016/j.cageo.2016.02.002.

Boutelier, D., Schrank, C., Regenauer-Lieb, K., 2019. 2-D finite displacements and strain from particle imaging velocimetry (PIV) analysis of tectonic analogue models with TecPIV. Solid Earth 10, 1123–1139. https://doi.org/10.5194/se-10-1123-2019.

Brun, J.-P., Sokoutis, D., 2007. Kinematics of the southern Rhodope core complex (North Greece). Int. J. Earth Sci. 96, 1079–1099. https://doi.org/10.1007/s00531-007-0174-2.

Brun, J.-P., Sokoutis, D., 2010. 45 my of Aegean crust and mantle flow driven by trench retreat. Geology 38, 815–818. https://doi.org/10.1130/G30950.1.

Brune, S., 2014. Evolution of stress and fault patterns in oblique rift systems: 3-D numerical lithospheric-scale experiments from rift to breakup. Geochem. Geophys. Geosyst. 15, 3392–3415. https://doi.org/10.1002/2014GC005446.

Brune, S., Corti, G., Ranalli, G., 2017. Controls of inherited lithospheric heterogeneity on rift linkage: numerical and analog models of interaction between the Kenyan and Ethiopian rifts across the Turkana depression. Tectonics 36, 1767–1786. https://doi.org/10.1002/2017TC004739.

Byerlee, J., 1978. Friction of rocks. In: Byerlee, J.D., Wyss, M. (Eds.), Rock Friction and Earthquake Prediction. Springer, pp. 615–626. https://doi.org/10.1007/978-3-0348-7182-2_4.

Cartwright, J.A., Trudgill, B.D., Mansfield, C.S., 1995. Fault growth by segment linkage: an explanation for scatter in maximum displacement and trace length data from the Canyonlands Grabens of SE Utah. J. Struct. Geol. 17, 1319–1326. https://doi.org/10.1016/0191-8141(95)00033-A.

Collanega, L., Jackson, C.A.-L., Bell, R., Coleman, A.J., Lenhart, A., Breda, A., 2018. How Do Intra-basement Fabrics Influence Normal Fault Growth? Insights from the Taranaki Basin, Offshore New Zealand. https://doi.org/10.31223/osf.io/8rn9u.

Corti, G., 2012. Evolution and characteristics of continental rifting: analog modeling-inspired view and comparison with examples from the East African Rift System. Tectonophysics 522, 1–33. https://doi.org/10.1016/j.tecto.2011.06.010.

Corti, G., Ranalli, G., Mulugeta, G., Agostini, A., Sani, F., Zugu, A., 2010. Control of the rheological structure of the lithosphere on the inward migration of tectonic activity during continental rifting. Tectonophysics 490, 165–172. https://doi.org/10.1016/j.tecto.2010.05.004.

Corti, G., Ranalli, G., Agostini, A., Sokoutis, D., 2013. Inward migration of faulting during continental rifting: effects of pre-existing lithospheric structure and extension rate. Tectonophysics 594, 137–148. https://doi.org/10.1016/j.tecto.2013.03.028.

Corti, G., Cioni, R., Franceschini, Z., Sani, F., Scaillet, S., Molin, P., Isola, I., Mazzarini, F., Brune, S., Keir, D., 2019. Aborted propagation of the Ethiopian rift caused by linkage with the Kenyan rift. Nat. Commun. 10, 1–11. https://doi.org/10.1038/s41467-019-09335-2.

Crameri, F., 2018. Scientific colour maps: perceptually uniform and colour-vision deficiency friendly. Zenodo. https://doi.org/10.5281/zenodo.1243862.

Dick, H.J., Lin, J., Schouten, H., 2003. An ultraslow-spreading class of ocean ridge. Nature 426, 405–412. https://doi.org/10.1038/nature02128.

Doré, A., Lundin, E., Jensen, L., Birkeland, Ø., Eliassen, P., Fichler, C., 1999. Principal tectonic events in the evolution of the northwest European Atlantic margin, geological society, London, petroleum geology conference series. In: Geological Society of London, pp. 41–61. https://doi.org/10.1144/0050041.

Ebinger, C., 2005. Continental break-up: the East African perspective. Astron. Geophys. 46, 2.16–12.21. https://doi.org/10.1111/j.1468-4004.2005.46216.x.

Gabrielsen, R.H., Sokoutis, D., Willingshofer, E., Faleide, J.I., 2016. Fault linkage across weak layers during extension: an experimental approach with reference to the Hoop Fault Complex of the SW Barents Sea. Pet. Geosci. 22, 123–135. https://doi.org/10.1144/petgeo2015-029.

Gabrielsen, R.H., Zalmstra, H., Sokoutis, D., Willingshofer, E., Faleide, J.I., Braut, H.L., 2019. The influence of mechanically weak layers in controlling fault kinematics and graben configurations: examples from analog experiments and the Norwegian continental margin. AAPG Bull. 103, 1097–1110. https://doi.org/10.1306/10261817077.

Glerum, A., Brune, S., Stamps, D.S., Strecker, M.R., 2020. Victoria continental microplate dynamics controlled by the lithospheric strength distribution of the East African Rift. Nat. Commun. 11, 1–15. https://doi.org/10.1038/s41467-020-16176-x.

Hanisch, J., 1984. The Cretaceous opening of the northeast Atlantic. Tectonophysics 101, 1–23. https://doi.org/10.1016/0040-1951(84)90039-8.

Heilman, E., Kolawole, F., Atekwana, E.A., Mayle, M., 2019. Controls of basement fabric on the linkage of rift segments. Tectonics 38, 1337–1366. https://doi.org/10.1029/2018TC005362.

Hubbert, M.K., 1937. Theory of scale models as applied to the study of geologic structures. Geol. Soc. Am. Bull. 48, 1459–1520. https://doi.org/10.1130/GSAB-48-1459.

Jackson, C.A.-L., Rotevatn, A., 2013. 3D seismic analysis of the structure and evolution of a salt-influenced normal fault zone: a test of competing fault growth models. J. Struct. Geol. 54, 215–234. https://doi.org/10.1016/j.jsg.2013.06.012.

Jackson, C.A.-L., Bell, R.E., Rotevatn, A., Tvedt, A.B., 2017. Techniques to determine the kinematics of synsedimentary normal faults and implications for fault growth models. Geol. Soc. Lond., Spec. Publ. 439, 187–217. https://doi.org/10.1144/SP439.22.

Khalil, H.M., Capitanio, F.A., Betts, P.G., Cruden, A.R., 2020. 3-D analog modeling constraints on rifting in the Afar region. Tectonics 39. https://doi.org/10.1029/2020TC006339 (e2020TC006339).

Klinkmüller, M., 2011. Properties of Analogue Materials, Experimental Reproducibility and 2D/3D Deformation Quantification Techniques in Analogue Modelling of Crustal-scale Processes. Verlag nicht ermittelbar.

Koehn, D., Aanyu, K., Haines, S., Sachau, T., 2008. Rift nucleation, rift propagation and the creation of basement micro-plates within active rifts. Tectonophysics 458, 105–116. https://doi.org/10.1016/j.tecto.2007.10.003.

Krézsek, C., Adam, J., Grujic, D., 2007. Mechanics of fault and expulsion rollover systems developed on passive margins detached on salt: insights from analogue modelling and optical strain monitoring. Geol. Soc. Lond., Spec. Publ. 292, 103–121. https://doi.org/10.1144/SP292.6.

Kydonakis, K., Brun, J.P., Sokoutis, D., 2015. North Aegean core complexes, the gravity spreading of a thrust wedge. J. Geophys. Res. 120, 595–616. https://doi.org/10.1002/2014JB011601.

Le Pourhiet, L., Chamot-Rooke, N., Delescluse, M., May, D.A., Watremez, L., Pubellier, M., 2018. Continental break-up of the South China Sea stalled by far-field compression. Nat. Geosci. 11, 605–609. https://doi.org/10.1038/s41561-018-0178-5.

Lundin, E., Doré, A., 1997. A tectonic model for the Norwegian passive margin with implications for the NE Atlantic: Early Cretaceous to break-up. J. Geol. Soc. 154, 545–550. https://doi.org/10.1144/gsjgs.154.3.0545.

Maestrelli, D., Montanari, D., Corti, G., Del Ventisette, C., Moratti, G., Bonini, M., 2020. Exploring the interactions between rift propagation and inherited crustal fabrics through experimental modeling. Tectonics 39. https://doi.org/10.1029/2020TC006211 (e2020TC006211).

Martin, A., 1984. Propagating rifts: crustal extension during continental rifting. Tectonics 3, 611–617. https://doi.org/10.1029/TC003i006p00611.

Michon, L., Merle, O., 2000. Crustal structures of the Rhinegraben and the Massif Central grabens: an experimental approach. Tectonics 19, 896–904. https://doi.org/10.1029/2000TC900015.

Molnar, N., Cruden, A., Betts, P., 2017. Interactions between propagating rotational rifts and linear rheological heterogeneities: insights from three-dimensional laboratory experiments. Tectonics 36, 420–443. https://doi.org/10.1002/2016TC004447.

Molnar, N.E., Cruden, A.R., Betts, P.G., 2018. Unzipping continents and the birth of microcontinents. Geology 46, 451–454. https://doi.org/10.1130/G40021.1.

Molnar, N.E., Cruden, A.R., Betts, P.G., 2019. Interactions between propagating rifts and linear weaknesses in the lower crust. Geosphere 15, 1617–1640. https://doi.org/10.1130/GES02119.1.

Molnar, N., Cruden, A., Betts, P., 2020. The role of inherited crustal and lithospheric architecture during the evolution of the Red Sea: insights from three dimensional analogue experiments. Earth Planet. Sci. Lett. 544, 116377 https://doi.org/10.1016/j.epsl.2020.116377.

Mondy, L.S., Rey, P.F., Duclaux, G., Moresi, L., 2018. The role of asthenospheric flow during rift propagation and breakup. Geology 46, 103–106. https://doi.org/10.1130/G39674.1.

Morley, C.K., 1999. Patterns of displacement along large normal faults: implications for basin evolution and fault propagation, based on examples from East Africa. AAPG Bull. 83, 613–634. https://doi.org/10.1306/00AA9C0A-1730-11D7-8645000102C1865D.

Morley, C., Nelson, R., Patton, T., Munn, S., 1990. Transfer zones in the East African rift system and their relevance to hydrocarbon exploration in rifts. AAPG Bull. 74, 1234–1253. https://doi.org/10.1306/0C9B2475-1710-11D7-8645000102C1865D.

Nelson, R., Patton, T., Morley, C., 1992. Rift-segment interaction and its relation to hydrocarbon exploration in continental rift systems. AAPG Bull. 76, 1153–1169. https://doi.org/10.1306/BDFF898E-1718-11D7-8645000102C1865D.

Nicol, A., Wallace, L., 2007. Temporal stability of deformation rates: comparison of geological and geodetic observations, Hikurangi subduction margin, New Zealand. Earth Planet. Sci. Lett. 258, 397–413. https://doi.org/10.1016/j.epsl.2007.03.039.

Nicol, A., Walsh, J., Berryman, K., Nodder, S., 2005. Growth of a normal fault by the accumulation of slip over millions of years. J. Struct. Geol. 27, 327–342. https://doi.org/10.1016/j.jsg.2004.09.002.

Nicol, A., Walsh, J., Villamor, P., Seebeck, H., Berryman, K., 2010. Normal fault interactions, paleoearthquakes and growth in an active rift. J. Struct. Geol. 32, 1101–1113. https://doi.org/10.1016/j.jsg.2010.06.018.

Panien, M., Schreurs, G., Pfiffner, A., 2006. Mechanical behaviour of granular materials used in analogue modelling: insights from grain characterisation, ring-shear tests and analogue experiments. J. Struct. Geol. 28, 1710–1724. https://doi.org/10.1016/j.jsg.2006.05.004.

Philippon, M., Brun, J.-P., Gueydan, F., Sokoutis, D., 2014. The interaction between Aegean back-arc extension and Anatolia escape since Middle Miocene. Tectonophysics 631, 176–188. https://doi.org/10.1016/j.tecto.2014.04.039.

Ramberg, H., 1981. Gravity, deformation and the earth's crust. In: Theory, Experiments and Geological Application. Academic Press.

Rotevatn, A., Jackson, C.A.-L., Tvedt, A.B., Bell, R.E., Blækkan, I., 2019. How do normal faults grow? J. Struct. Geol. 125, 174–184. https://doi.org/10.1016/j.jsg.2018.08.005.

Schellart, W.P., Strak, V., 2016. A review of analogue modelling of geodynamic processes: approaches, scaling, materials and quantification, with an application to subduction experiments. J. Geodyn. 100, 7–32. https://doi.org/10.1016/j.jog.2016.03.009.

Schellart, W.P., Lister, G.S., Jessell, M.W., 2002. Analogue modelling of asymmetrical back-arc extension. J. Virtual Explor. 7, 25–42. https://doi.org/10.3809/jvirtex.2002.00046.

Schellart, W.P., Jessell, M., Lister, G., 2003. Asymmetric deformation in the backarc region of the Kuril arc, northwest Pacific: new insights from analogue modeling. Tectonics 22. https://doi.org/10.1029/2002TC001473.

Schlagenhauf, A., Manighetti, I., Malavieille, J., Dominguez, S., 2008. Incremental growth of normal faults: insights from a laser-equipped analog experiment. Earth Planet. Sci. Lett. 273, 299–311. https://doi.org/10.1016/j.epsl.2008.06.042.

Schlische, R., 1992. Rift Basin Evolution and the Growth of Normal Faults. Geological Society of America, p. 24. Abstracts with Programs;(United States).

Schmid C., T., Rudolf, M., Schreurs, G., Adam, J., Rosenau, M., 2021. 3D stereo DIC data from analogue models exploring fault growth and rift propagation in rotational rift systems. GFZ Data Services. https://doi.org/10.5880/fidgeo.2021.048.

Schmid, T., Schreurs, G., Warsitzka, M., Rosenau, M., 2020a. Effect of Sieving Height on Density and Friction of Brittle Analogue Material: Ring-shear Test Data of Corundum Sand Used for Analogue Experiments in the Tectonic Modelling Lab of the University of Bern (CH). GFZ Data Services. https://doi.org/10.5880/fidgeo.2020.005.

Schmid, T., Schreurs, G., Warsitzka, M., Rosenau, M., 2020b. Effect of Sieving Height on Density and Friction of Brittle Analogue Material: Ring-shear Test Data of Quarz Sand Used for Analogue Experiments in the Tectonic Modelling Lab of the University of Bern. GFZ Data Services. https://doi.org/10.5880/fidgeo.2020.006.

Schueller, S., Gueydan, F., Davy, P., 2005. Brittle-ductile coupling: role of ductile viscosity on brittle fracturing. Geophys. Res. Lett. 32. https://doi.org/10.1029/2004GL022272.

Seebeck, H., Nicol, A., Villamor, P., Ristau, J., Pettinga, J., 2014. Structure and kinematics of the Taupo Rift, New Zealand. Tectonics 33, 1178–1199. https://doi.org/10.1002/2014TC003569.

Sekretov, S.B., 2001. Eurasian Basin-Laptev Sea geodynamic system: tectonic and structural evolution. Polarforschung 69, 51–54.

Smith, J.V., 1993. Infinitesimal kinematics of rotational rifting with reference to en echelon marginal faults in the Red Sea region. Tectonophysics 222, 227–235. https://doi.org/10.1016/0040-1951(93)90050-T.

Souriot, T., Brun, J.-P., 1992. Faulting and block rotation in the Afar triangle, East Africa: the Danakil" crank-arm" model. Geology 20, 911–914. https://doi.org/10.1130/0091-7613(1992)020<0911:FABRIT>2.3.CO;2.

Thielicke, W., Stamhuis, E., 2014. PIVlab–towards user-friendly, affordable and accurate digital particle image velocimetry in MATLAB. J. Open Res. Softw. 2. https://doi.org/10.5334/jors.bl.

Van Wijk, J., Blackman, D., 2005. Dynamics of continental rift propagation: the end-member modes. Earth Planet. Sci. Lett. 229, 247–258. https://doi.org/10.1016/j.epsl.2004.10.039.

Vasquez, L., Nalpas, T., Ballard, J.-F., De Veslud, C.L.C., Simon, B., Dauteuil, O., Du Bernard, X., 2018. 3D geometries of normal faults in a brittle-ductile sedimentary cover: analogue modelling. J. Struct. Geol. 112, 29–38. https://doi.org/10.1016/j.jsg.2018.04.009.

Villamor, P., Berryman, K., 2006. Evolution of the southern termination of the Taupo Rift, New Zealand. N. Z. J. Geol. Geophys. 49, 23–37. https://doi.org/10.1080/00288306.2006.9515145.

Villamor, P., Berryman, K., Ellis, S., Schreurs, G., Wallace, L., Leonard, G., Langridge, R., Ries, W., 2017. Rapid evolution of subduction-related continental intraarc rifts: the Taupo Rift, New Zealand. Tectonics 36, 2250–2272. https://doi.org/10.1002/2017TC004715.

Wallace, L.M., Beavan, J., McCaffrey, R., Darby, D., 2004. Subduction zone coupling and tectonic block rotations in the North Island, New Zealand. J. Geophys. Res. 109. https://doi.org/10.1029/2004JB003241.

Wallace, L.M., McCaffrey, R., Beavan, J., Ellis, S., 2005. Rapid microplate rotations and backarc rifting at the transition between collision and subduction. Geology 33, 857–860. https://doi.org/10.1130/G21834.1.

Wallace, L.M., Ellis, S., Mann, P., 2009. Collisional model for rapid fore-arc block rotations, arc curvature, and episodic back-arc rifting in subduction settings. Geochem. Geophys. Geosyst. 10. https://doi.org/10.1029/2008GC002220.

Walsh, J.J., Watterson, J., 1988. Analysis of the relationship between displacements and dimensions of faults. J. Struct. Geol. 10, 239–247. https://doi.org/10.1016/0191-8141(88)90057-0.

Walsh, J., Nicol, A., Childs, C., 2002. An alternative model for the growth of faults. J. Struct. Geol. 24, 1669–1675. https://doi.org/10.1016/S0191-8141(01)00165-1.

Walsh, J., Bailey, W., Childs, C., Nicol, A., Bonson, C., 2003. Formation of segmented normal faults: a 3-D perspective. J. Struct. Geol. 25, 1251–1262. https://doi.org/10.1016/S0191-8141(02)00161-X.

Watterson, J., 1986. Fault dimensions, displacements and growth. Pure Appl. Geophys. 124, 365–373. https://doi.org/10.1007/BF00875732.

Weijermars, R., Schmeling, H., 1986. Scaling of Newtonian and non-Newtonian fluid dynamics without inertia for quantitative modelling of rock flow due to gravity (including the concept of rheological similarity). Phys. Earth Planet. Inter. 43, 316–330. https://doi.org/10.1016/0031-9201(86)90021-X.

Westerweel, J., Scarano, F., 2005. Universal outlier detection for PIV data. Exp. Fluids 39, 1096–1100. https://doi.org/10.1007/s00348-005-0016-6.

Zwaan, F., Schreurs, G., 2017. How oblique extension and structural inheritance influence rift segment interaction: insights from 4D analog models. Interpretation 5, SD119–SD138. https://doi.org/10.1190/INT-2016-0063.1.

Zwaan, F., Schreurs, G., 2020. Rift segment interaction in orthogonal and rotational extension experiments: implications for the large-scale development of rift systems. J. Struct. Geol. 140, 104119 https://doi.org/10.1016/j.jsg.2020.104119.

Zwaan, F., Schreurs, G., Naliboff, J., Buiter, S.J., 2016. Insights into the effects of oblique extension on continental rift interaction from 3D analogue and numerical models. Tectonophysics 693, 239–260. https://doi.org/10.1016/j.tecto.2016.02.036.

Zwaan, F., Schreurs, G., Adam, J., 2017. Effects of sedimentation on rift segment and transfer zone evolution in orthogonal and oblique extension settings: insights from analogue models analysed with 4D X-ray computed tomography and digital volume correlation techniques. Glob. Planet. Chang. 171, 110–133. https://doi.org/10.1016/j.gloplacha.2017.11.002.

Zwaan, F., Schreurs, G., Ritter, M., Santimano, T., Rosenau, M., 2018. Rheology of PDMS-corundum sand mixtures from the Tectonic Modelling Lab of the University of Bern (CH). GFZ Data Services. https://doi.org/10.5880/fidgeo.2018.023.

Zwaan, F., Schreurs, G., Buiter, S.J.H., 2019. A systematic comparison of experimental set-ups for modelling extensional tectonics. Solid Earth 10, 1063–1097. https://doi.org/10.5194/se-10-1063-2019.

Zwaan, F., Schreurs, G., Rosenau, M., 2020. Rift propagation in rotational versus orthogonal extension: insights from 4D analogue models. J. Struct. Geol. 135, 103946 https://doi.org/10.1016/j.jsg.2019.103946.